

Beyond the Visible: A Survey on Cross-spectral Face Recognition

David Anghelone, Cunjian Chen, Arun Ross, Antitza Dantcheva

Abstract—Cross-spectral face recognition (CFR) refers to recognizing individuals using face images stemming from different spectral bands, such as infrared vs. visible. While CFR is inherently more challenging than classical face recognition due to significant variation in facial appearance caused by the *modality gap*, it is useful in many scenarios including night-vision biometrics and detecting presentation attacks. Recent advances in convolutional neural networks (CNNs) have resulted in significant improvement in the performance of CFR systems. Given these developments, the contributions of this survey are three-fold. First, we provide an overview of CFR, by formalizing the CFR problem and presenting related applications. Secondly, we discuss the appropriate spectral bands for face recognition and discuss recent CFR methods, placing emphasis on *deep neural networks*. In particular we describe techniques that have been proposed to extract and compare heterogeneous features emerging from different spectral bands. We also discuss the datasets that have been used for evaluating CFR methods. Finally, we discuss the challenges and future lines of research on this topic.

Index Terms—Biometrics, Cross-spectral, Face recognition, Deep neural networks, Infrared, Thermal

arXiv:2201.04435v2 [cs.CV] 6 May 2022

1 INTRODUCTION

Face Recognition (FR) has been a very active research field for the last several decades [1], [2], [3], [4]. Advances in deep convolutional neural networks (CNNs) and the associated seminal work on DeepFace [5] have brought significant progress in this area, tackling a number of challenges including variations in pose, illumination and expression (PIE), as well as resolution and unconstrained settings. While such work have predominantly focused on the visible (VIS) spectrum, considering additional spectra allows for increased robustness [6], [7], in particular in the presence of different *poses*, *illumination variations*, *noise*, as well as *occlusions*. Further benefits include incorporating the *absolute size of objects*, as well as *robustness to presentation attacks* such as the use of makeup and masks to circumvent a system [8]. Therefore, comparing RGB face images against face images acquired beyond the visible spectrum, often referred to as Cross-spectral Face Recognition (CFR), is of particular significance in designing FR systems for *defense*, *surveillance*, and *public safety* [6] and falls under the broader category of Heterogeneous Face Recognition (HFR). Here, *heterogeneous* indicates that face images have been acquired in different sensing modalities e.g., visible, infrared, 3D, and hand-drawn sketches (see Figure 1).

We note that CFR is more challenging than traditional FR for both *human examiners* as well as *computer vision algorithms*. This is due to following three factors. Firstly, large *intra-spectral variation*, where within the same modality, face samples of the same subject can exhibit larger appearance variations than face samples of different subjects. Secondly, the *modality gap* is of concern, where appearance



Fig. 1: Examples of **heterogeneous face images** of the same subject captured in different modalities, i.e., domains. Images are from the Tufts dataset [9].

variation between two face samples of the same subject can be larger than that of two samples belonging to two different subjects (see Figure 1). This can result in degraded face recognition performance. Finally, the *limited* availability of *training samples* of cross-modality face image pairs can make it difficult to design effective CFR methods using deep neural networks.

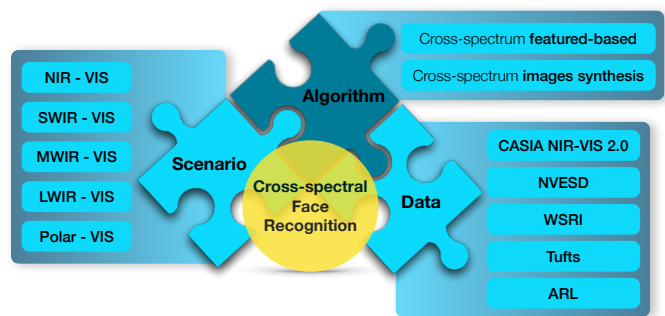


Fig. 2: An overview of cross-spectral face recognition

Recent advances in CNNs and generative adversarial networks (GANs) have allowed for remarkable improvements in CFR [10], [11], [12], [13]. The goal of this survey

- D. Anghelone and A. Dantcheva are with the STARS team of Inria, France. E-mail: {david.anghelone, antitza.dantcheva}@inria.fr
- C. Chen and A. Ross are with the Department of Computer Science and Engineering at Michigan State University (MSU). E-mail: cunjian@msu.edu, rossarun@cse.msu.edu

Manuscript received ; revised .

article is to provide an overview of these advances. Specifically, we describe the proposed methods, used datasets, as well as the results and associated insights. In this context, we consider the electromagnetic spectrum ranging from near infrared (NIR) to more challenging bands such as mid-wave infrared (MWIR) and longwave infrared (LWIR), as illustrated in Figure 2. Unlike other introductory overview articles including [6], [14], [15], we focus on highlighting recent advances based on *deep learning* in addressing CFR, and techniques that have been developed to bridge the modality gap.

The remainder of this paper is organized as follows. We formalize CFR in Section 2 and present some applications in Section 3. We discuss the various spectral bands, i.e., sensing modalities, that are relevant to face recognition, in Section 4. In Section 5 we describe the general modules of a CFR system, viz., face image pre-processing and feature extraction. The various deep learning based CFR methods that have been proposed in the literature are explained in Section 6 and 7, while the relevant datasets used for research in this field are presented in Section 8. Finally, in Section 9, we discuss open research problems that are currently being addressed in the field of CFR.

2 FORMALIZATION OF CFR

Inspired by previous work [16], [17], we firstly formalize the FR-task and then the CFR-task as follows.

Let \mathcal{M} be an electromagnetic spectral space modality associated with a marginal distribution \mathbb{P} over a d -dimensional feature space $\mathcal{X} \subset \mathbb{R}^d$ and a label space $\mathcal{Y} \subset \mathbb{N}$.

Given a n -face database $X = \{\mathbf{x}_i\}_{i=1}^n$, where $\mathbf{x}_i \in \mathcal{X}$, and their corresponding n -identities $Y = \{y_j\}_{j=1}^n$ ($y_j \in \mathcal{Y}$), a FR-model is defined as a parametric function $\mathcal{F}_{FR,\Theta}$ described by the random variables X (feature space), Y (label space) and deep learning model parameters, Θ , which extract features from a CNN.

$$\mathcal{F}_{FR,\Theta} : \begin{array}{l} X \times Y \rightarrow [0, 1] \\ (\mathbf{x}_i, y_j) \mapsto \mathbb{P}(Y = y_j | X = \mathbf{x}_i, \Theta), \end{array} \quad (1)$$

where, $i, j \in [1, n]$.

Thus, the FR-model aims to deduce parameters, Θ , that increase the probability of correct recognition to 1, assuming that the correct face is in the gallery. More specifically, for all k -index identities $\in [1, n]$

$$\mathcal{F}_{FR,\Theta}(\mathbf{x}_k, y_k) = \mathbb{P}(Y = y_k | X = \mathbf{x}_k, \Theta) = 1. \quad (2)$$

However, in the case of CFR, we compare acquired face images in two different modalities (or spectra or domains): the source \mathcal{M}^s and the target \mathcal{M}^t . Each of them is associated with a marginal distribution \mathbb{P} over the d -dimensional feature space for both source $X^s = \{\mathbf{x}_i^s\}_{i=1}^n \subset \mathcal{X}^s$ and target $X^t = \{\mathbf{x}_i^t\}_{i=1}^n \subset \mathcal{X}^t$, respectively. Note that they share the same set of labels $Y = \{y_j\}_{j=1}^n \subset \mathcal{Y}$.

The CFR-function, $\mathcal{F}_{CFR,\Theta}$, is formalized as follows. Towards finding the deep learning model parameters, Θ , for all k -index identities $\in [1, n]$, we have

$$\mathbb{P}(Y = y_k | X^s = \mathbf{x}_k^s, \Theta) = \mathbb{P}(Y = y_k | X^t = \mathbf{x}_k^t, \Theta) = t, \quad (3)$$

where, $t \in [0, 1]$ is a predefined threshold.

Algorithms reviewed in this paper seek to provide strategies for determining Θ , formalized in Equation (3).

During enrollment, a *gallery face image* is captured and processed and being stored as *reference template*, representing the biometric information of an individual. At the time of authentication, a *probe face image* is captured and processed in the same way as in the enrollment and compared against a reference template of a claimed identity (verification) or against all stored reference templates (identification) [18].

Mathematically, both heterogeneous verification and identification are formalized as follows. The user is either *genuine* – the claim is true, or an *impostor* – the claim is false. They are represented by the set $\Omega = \{\omega_{true}, \omega_{false}\}$, respectively.

In CFR-verification, an input feature vector $\mathbf{x}_q^t \in \mathcal{X}^t$ stemming from the target modality \mathcal{M}^t and a claimed identity $y_j \in \mathcal{Y}$ are embedded as the pair (\mathbf{x}_q^t, y_j) . The comparison algorithm (Section 5.2) analyzes the extracted templates \mathbf{x}_q^t , and a function \mathcal{S} (Section 5.3) computes a *similarity score* (11) according to the stored source template $\mathbf{x}_j^s \in X^s$. If the score exceeds a predefined threshold t , it is considered a match. Thus,

$$(\mathbf{x}_q^t, y_j) \in \begin{cases} \omega_{true}, & \text{if } \mathcal{S}(\mathbf{x}_j^s, \mathbf{x}_q^t) \geq t \\ \omega_{false}, & \text{otherwise.} \end{cases} \quad (4)$$

In CFR-identification, an input feature vector $\mathbf{x}_q^t \in \mathcal{X}^t$ derived from the target modality \mathcal{M}^t is provided to the biometric system. The system attempts to search in the gallery for the appropriate identity y_k correlated with $\mathbf{x}_k^s \in X^s$, where $k \in [1, n]$. The associated template is able to provide the highest similarity score (11). In addition, the highest score exceeding the predefined threshold t leads to a match. Otherwise the user is classified as unknown $y_{unknown}$. Thus,

$$\mathbf{x}_q^t \in \begin{cases} y_k, & \text{if } \max_{k \in [1, n]} \{\mathcal{S}(\mathbf{x}_k^s, \mathbf{x}_q^t) \geq t\} \\ y_{unknown}, & \text{otherwise.} \end{cases} \quad (5)$$

3 APPLICATIONS OF CFR

FR-systems have been widely deployed and operate mainly in the visible spectrum [19], due to the ubiquity of low-cost cameras. As motivated in the introduction, CFR-systems have been beneficial in additional applications, for example, in *Intelligence Video Surveillance (IVS)*. Beyond *access control*, the application of CFR has strong potential to provide new capabilities in *law enforcement*, *military* and the *AI community*, especially for commercial purposes.

A pertinent application for CFR has been in law enforcement and homeland security [20]. In this context, IR-sensors can be used for long-range monitoring and capturing biometric modalities at variable standoff distances, as well as in low-light and night-time scenarios. In such cases, the acquired image often has to be compared against a gallery consisting of visible spectrum face images. Similar applications are found in military settings involving identifying individuals in challenging environments [7]. On a wider scale, HFR (which is a superset of CFR) is beneficial for deflecting presentation attacks [21], [22] or for sketch-visual identification, e.g., finding an individual whose appearance

was sketched and whose face image may be present in a mugshot suspect database [23].

4 DIFFERENT SPECTRA

We next proceed to introduce the infrared (IR) spectral bands, which we illustrate in Figure 3, that have been employed in CFR.

Wolff *et al.* [24], Buddharaju *et al.* [25], Kong *et al.* [26], Bhowmik *et al.* [27], and Bourlai and Hornak [7] describe *infrared light* as an invisible, heat-associated energy that can be sensed when radiation or warmth are reflected or emitted from an object. Unlike ultraviolet rays [28], IR-waves penetrate the skin without damage to health. We note that, in principle, IR sensors capture either the *face-reflection* of infrared light or the *heat face-emission* stemming from the subcutaneous superficial blood vessels. In particular, face contains blood capillaries and forms a subcutaneous network. More physiology-details including the uniqueness of individual's physiology can be found in the work of Buddharaju *et al.* [25].

IR bands have been defined according to the standard ISO-20473:2007 as near-infrared (NIR) between 0.78–3 μm , mid-infrared (MIR) between 3–50 μm and far-infrared (FIR) 50–1000 μm . Deviating from that, the CIE-International Commission on Illumination has divided the IR-spectrum into the bands IR-A (0.7 μm – 1.4 μm), IR-B (1.4 μm – 3 μm) and IR-C (3 μm – 1000 μm).

In this paper, we use a division of the IR bands based on physical properties, which determine **reflection-dominated** and **emission-dominated** regions. These regions, also denoted as *Passive* and *Active* IR, respectively, are further divided into sub-spectra, which we summarize in Figure 3. We note that a similar scheme has been employed by manufacturers of IR sensors, where specific sensors have been developed, associated to active or passive IR.

Experiment 1. In order to demonstrate the modality gap, we conduct the following experiment inspired by Hu *et al.* [6]. We select heterogeneous images pertaining to one subject from the Tufts dataset [9]. For the HFR scenarios *Visible/Visible*, *Visible/NIR*, *Visible/LWIR* and *Visible/Sketch*, we compute associated structural similarity (SSIM) scores. Towards evaluating the modality gap in CFR, the SSIM metric (6), as proposed by Wang *et al.* (2004) [29], has been widely accepted. In our context, SSIM indicates the similarity between a visible spectrum reference image x and a gallery image y (in our case infrared) by assessing the perturbation of structural information caused by factors such as luminance and contrast. Specifically,

$$SSIM(x, y) = \frac{(2\mu_x\mu_y + c_1)(2\sigma_{xy} + c_2)}{(\mu_x^2 + \mu_y^2 + c_1)(\sigma_x^2 + \sigma_y^2 + c_2)}, \quad (6)$$

where, μ , and σ , denote mean and standard deviation, respectively, and σ_{xy} represents the covariance of the respective images. Here, c_1 and c_2 are constants. SSIM (6) ranges between -1 and 1 , with 1 being the extreme case, when compared images x and y are identical.

The structural similarity maps and associated SSIM-scores computed in Experiment 1 are illustrated in Figure 5, highlighting face-areas that are most sensitive to

infrared energies. While the wavelength in the infrared band increases, the SSIM-difference increases as well. We observe different emission patterns around nose, mouth and eyes (blue panel). Furthermore, the results suggest that the largest challenges (lowest SSIM-scores) have to do with comparing an image in the visible spectrum with a sketch as well as with a thermal image. In both cases, we obtain similar SSIM-scores.

4.1 Active IR

The active IR region comprises of *near infrared* (NIR) and *shortwave infrared* (SWIR), characterized by reflective material properties, which require an (invisible) IR light to reveal the scene.

NIR is placed right next to the red-channel of the visible spectrum, with increased wavelength, which is exhibited in the visual similarities between VIS and NIR images (Figure 1). We observe this in Experiment 1 when comparing *VIS-NIR* faces, where the SSIM score is 0.479 (Figure 5). NIR is instrumental in CFR, as it remains invariant to lighting-direction and low-light conditions and, hence, is employed for monitoring and night-surveillance [30].

SWIR-imagery, similar to NIR, is visually close to visible imagery. See Figure 4. The SWIR-band is significantly wider than the NIR-band and enables sensing in atmospherically challenging conditions such as *rain*, *fog*, *mist*, *haze*, and common urban particulates such as *smoke* and *pollution* [27]. In addition, SWIR-sensors are able to capture objects in extremely low-light conditions, which renders SWIR suitable for surveillance, allowing for long-range applications (< 1 km) [31], as well as for identification purposes [32].

4.2 Passive IR

Beyond a wavelength of $\lambda = 3\mu\text{m}$, the IR band is significantly emissive and aims to acquire heat-sensitive radiation emitted from a human face. Hence, thermal sensors can be designed to capture temperature variations across the facial skin tissue due to the underlying face vasculature [25]. One of the benefits of the emission-dominated regions are that thermal imagery can be passively acquired without any external illumination, in either day or night environments [24]. Passive IR is comprised of Midwave (MWIR) and Longwave (LWIR). Note however that the range between MWIR and LWIR (ranging between $\lambda = 5\mu\text{m} - 8\mu\text{m}$, see Figure 3) constitutes a strong atmospheric absorption window rendering image acquisition impossible.

MWIR is located between SWIR and LWIR, and has both reflective and emissive properties - allowing for the sensing of different facial-skin-features including vein patterns [33]. However, it is the emissive component that is predominantly exploited in CFR, which is why face images captured in MWIR tend to largely resemble heat face signatures, and are visually distinct from visible imagery (see Figure 4).

LWIR extends the infrared band up to $\lambda = 14\mu\text{m}$ and consists of exclusively emitted radiation. This shift introduces high within-class variations and notably impedes a match with visible images (Figure 4). We observe that *Vis-LWIR* is the most challenging scenario as per Figure 5, with the lowest SSIM score of 0.251. LWIR imagery is visually similar to that of MWIR with respect to shape and contrast (Figure 4).

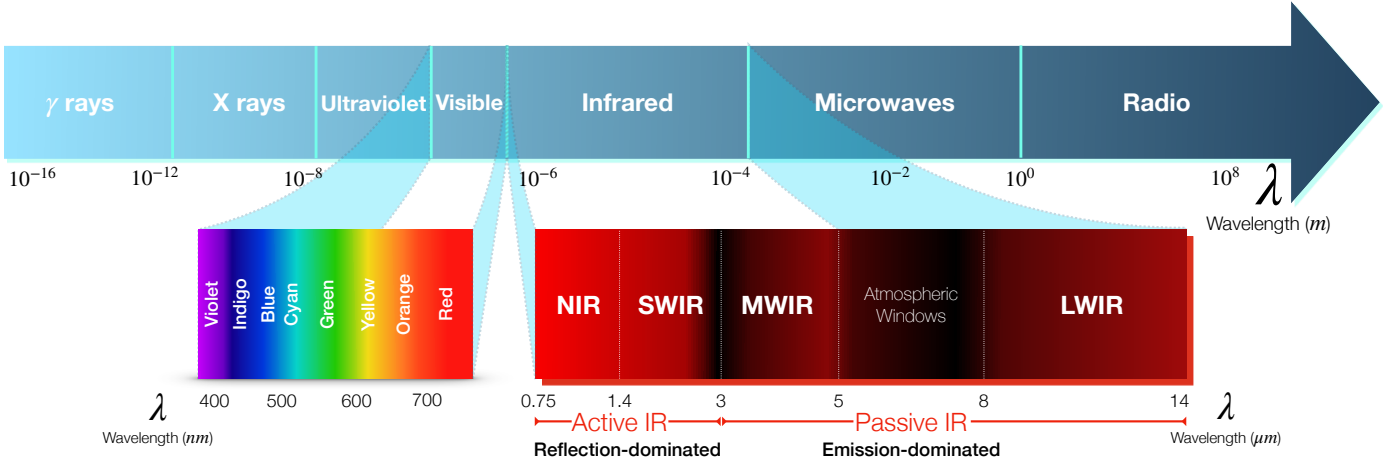


Fig. 3: **Electromagnetic spectrum.** Modalities and their associated wavelengths, highlighting the visible and infrared radiations.



Fig. 4: **Face beyond the visible.** A comparison of a face in visible (VIS) and infrared bands, viz., NIR, SWIR, MWIR and LWIR. We note the different physiological properties in both **Active IR** (NIR, SWIR) and **Passive IR** (MWIR, LWIR) bands. Figure credit: Hu *al.* [6]

infrared spectrum, as well as in any other spectrum. By performing optical filtering of the light at precise rotational angles, say $0^\circ, 90^\circ, 45^\circ$ and -45° related to the horizontal axes, more geometrical and textural details are obtained, which is able to enhance the conventional intensity-based thermal images for face recognition purposes. Towards inferring polarimetric-information in the passive IR and capturing the thermal radiance, specific infrared polarimetric sensors have been used. Through light manipulation, the polarization state information is typically expressed in terms of *Stokes parameters* \vec{S} , as firstly introduced by G. Stokes in 1852. For more details, the reader is referred to the work of Pezzaniti and Chenault [34]. \vec{S} is derived from the following linear combination.

$$\vec{S} = \begin{bmatrix} S_0 \\ S_1 \\ S_2 \\ S_3 \end{bmatrix} = \begin{bmatrix} I_0^\circ + I_{90}^\circ \\ I_0^\circ - I_{90}^\circ \\ I_{45}^\circ + I_{-45}^\circ \\ I_R^\circ + I_L^\circ \end{bmatrix}, \quad (7)$$

where, I_0° and I_{90}° denote the horizontal and vertical polarized light, respectively, while I_{45}° and I_{-45}° represent the diagonal polarized light and I_R° and I_L° , respectively, represent the intensity of the right and left circularly polarized light. The *Stokes parameter*, S_0 , represents the conventional thermal images without polarization information, S_1 and S_2 convey orthogonal polarimetric information and display additional details. Finally, S_3 is considered to be 0 in most applications, due to lack of circular information in the thermal spectrum. The degree of linear polarization (DoLP) can then be computed as

$$DoLP = \frac{\sqrt{S_1^2 + S_2^2}}{S_0}, \quad (8)$$

and it denotes the spectral radiation window of the electromagnetic spectrum which is linearly polarized. The polarimetric image entails the channel combinations of S_0, S_1 , and S_2 (see Figure 6).

Experiment 2. We compute SSIM scores between *Visible* and *Thermal* images (including each polarization state and degree of linear polarization), which we report in Table

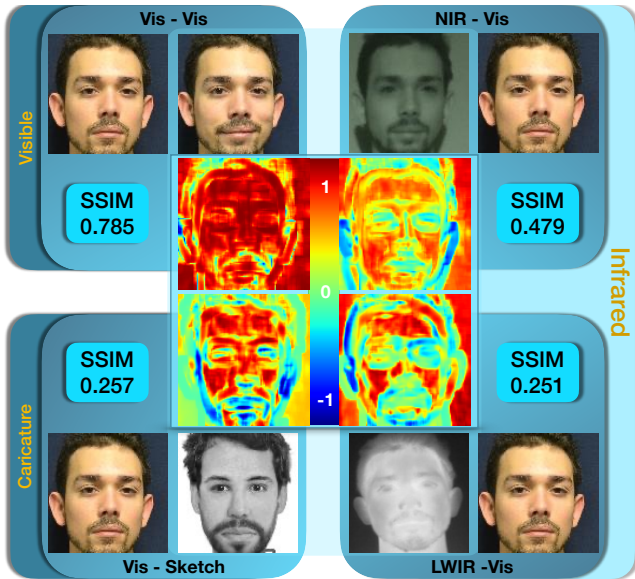


Fig. 5: **Structure Similarity (SSIM) maps and scores.** A visualization strategy to understand the human and machine visual perception when comparing two images in different scenarios: *Visible* - against *Visible/NIR/LWIR/Sketch*.

4.3 Polarimetric thermal imagery

Polarimetric thermal imagery aims to measure the polarization state information of the light contained in the thermal

1. The scores confirm the improvement due to the use of *polarimetric* thermal imagery. We note that SSIM pertaining to polarimetric imagery, outperforms the one due to thermal imagery. Therefore, polarimetric thermal imagery can facilitate CFR, which will be later confirmed in Section 5.3.

TABLE 1: **Experiment 2.** Computation of cosine similarity scores using state-of-the-art face matchers and structural similarity SSIM for images depicted in Figure 6. The scores are normalized to [0,1].

Face Matchers	Vis/ Vis	Stokes parameters			Channel combinations	
		S_0	S_1	S_2	DoLP	Vis/ Polar
SphereFace [35]	1.0	0.499	0.473	0.486	0.461	0.698
AM-Softmax [10]	1.0	0.543	0.576	0.555	0.596	0.702
MobileFaceNet [10]	1.0	0.505	0.499	0.503	0.507	0.702
ArcFace [36]	1.0	0.641	0.658	0.587	0.67	0.684
SSIM	1.0	0.286	0.236	0.262	0.209	0.300

5 CROSS-SPECTRAL FACE RECOGNITION

As in classical face recognition, *face detection* and *alignment* are considered the first and foremost steps of CFR. CFR data is preprocessed by aligning and cropping faces to reference templates based on detected facial landmarks. Then, a standard pipeline proceeds in learning/extracting face features by using optimal network architectures and loss functions.

5.1 Face Preprocessing

Very limited work has focused on facial landmark detection beyond the visible spectrum [37], [38], [39]. Since NIR and SWIR face images closely resemble visible spectrum faces, landmark detection methods developed for visible face images are directly applicable.

Experiment 3. Towards demonstrating the possibility of adapting landmark detection methods developed for the visible spectrum, we utilize MTCNN [40] to perform face detection and landmark detection experiments on NIR faces. Next, an affine transformation is computed based on the detected landmarks to normalize the detected faces to a frontal pose (see Figure 7).

As demonstrated, while it might be relatively easy to perform landmark detection on NIR or SWIR face images, it remains a challenge in the context of thermal face images, including MWIR and LWIR. We note that thermal face images tend to have lower contrast, lower resolution and lack texture information [37]. Poster et al. [37] analyzed the performances of three modern deep learning based landmark detection methods on thermal face images, namely *Deep Alignment Network* (DAN), *Multi-Task CNN* (MTCNN), and *multi-class patch based fully CNN* (PBC). These landmark detection algorithms were evaluated on the *ARL polarimetric thermal face* dataset [42] with 5-landmarks. Kopaczka et al. [38] assembled a high-resolution thermal facial image dataset in the LWIR spectral band and manually annotated 68 landmark points. DAN was used as the representative deep learning landmark detector to train and evaluate on the assembled dataset. Chu and Liu [39] proposed to use U-Net as a backbone to detect 68 facial landmarks on the same dataset used in [38]. The landmark detection task was designed as a multi-task learning framework by integrating emotion recognition. Poster et al. [43] used a coupled convolutional network architecture to leverage visible face data to train a thermal-only face landmark detection model.

Examples of 68-point ground-truth landmark annotations are depicted in Figure 8.

5.2 Deep Feature Extraction

After face images are preprocessed, two different schemes can be leveraged to compute domain-invariant features. Firstly, faces from different spectral bands can be directly ingested by a CNN, aiming to learn a shared feature representation scheme. Secondly, faces can be transformed by GANs into a target domain and features can be extracted from the transformed images.

5.2.1 Convolutional Neural Networks (CNNs)

CNNs are a class of neural networks that are highly efficient in learning effective feature representations for FR [10], [35], [36]. For CFR, CNNs operate on specific pairs of data, e.g., NIR-VIS, formed by different spectral bands. Depending on the number of pairs, CNNs can be designed with a two-branch [44], [45], [46] or a three-branch architecture [47]. Weights from individual branches are often shared. An example of such a design is depicted in Figure 9. Visible and NIR images represent respectively input to the network, extracting features. To learn domain-invariant features that are independent of the given spectral bands, a contrastive loss function is applied to enforce the identity constraint for these two extracted feature vectors [44]. For triplet inputs formed by anchor, positive and negative samples, a triplet loss is generally applied to minimize the gap between different spectral bands [47]. There are several prominent CNN-architectures that can be used as backbone for the architecture in Figure 9, some of which we enlist in Table 2.

TABLE 2: **Representative architectures** used in CFR for both CNNs and GANs.

Year	Backbone Architecture	Source	Used in
2014	VGGNet	[48]	[16], [49], [50], [51]
	GoogLeNet	[52]	[44]
2015	ResNet	[53]	[54], [55], [56]
2015	U-Net	[57]	[58], [59], [60], [61]
2016	Inception-ResNet	[62]	[16], [63], [64]
2017	DenseNet	[65]	[11], [66]
2018	LightCNN	[67]	[12], [16], [45], [46], [47], [56], [68]

5.2.2 Generative Adversarial Networks (GANs)

GANs are deep learning frameworks introduced by Goodfellow et al. [69] (2014), which consist of two sub-networks, a *Generative* model G and a *Discriminative* model D trained simultaneously. Together, G and D compete with each other in a minimax game. Specifically, G aims to learn the intrinsic distribution p_G over some target data $x \sim p_{data}$, and associated with a noise prior $z \sim p_z$. G draws sample z for creating synthetic data $G(z)$. In the meantime, D aids the training by taking x or $G(z)$ as input and performing a binary classification as to whether the input is from the real data distribution p_{data} or from the generated data distribution p_G . G attempts to mislead D to not be able to distinguish generated images from real, while D attempts to make that distinction.

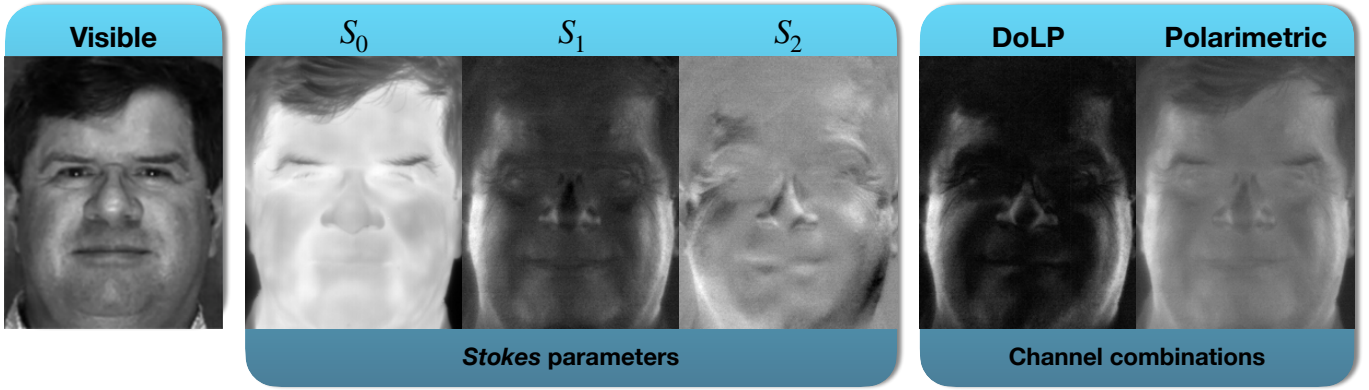


Fig. 6: **Stokes parameters.** Example images of a subject captured in the visible spectrum and their corresponding conventional thermal S_0 , polarization state information S_1 and S_2 , and polarimetric thermal images. Related SSIM-scores are reported in Table 1.

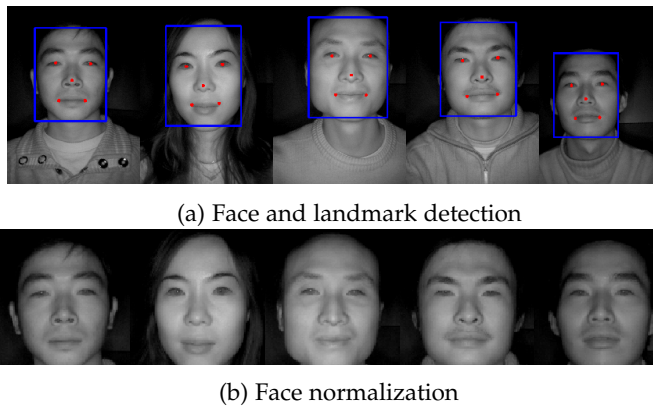


Fig. 7: **Experiment 3.** Face and landmark detection experiments conducted on near-infrared faces sampled from [41]. Face normalization was performed by aligning the faces to the reference pose based on the detected landmarks.



Fig. 8: **Landmark detection in thermal imagery.** Example images from a thermal dataset [38] showing 68-point ground-truth landmark annotations.

The optimization competition of these two models results in the following minimax game

$$\min_G \max_D \mathbb{E}_{x \sim p_{data(x)}} [\log(D(x))] + \mathbb{E}_{z \sim p_z} [\log(1 - D(G(z)))]. \tag{9}$$

Traditional GANs learn a mapping from a random noise input z to an output image y , while conditional GANs learn the mapping from an observed image x and a random noise z in which both G and D are conditioned to an output image y according to

$$\min_G \max_D \mathbb{E}_{x \sim p_{data(x)}} [\log(D(x|y))] + \mathbb{E}_{z \sim p_z} [\log(1 - D(G(z|y)))]. \tag{10}$$

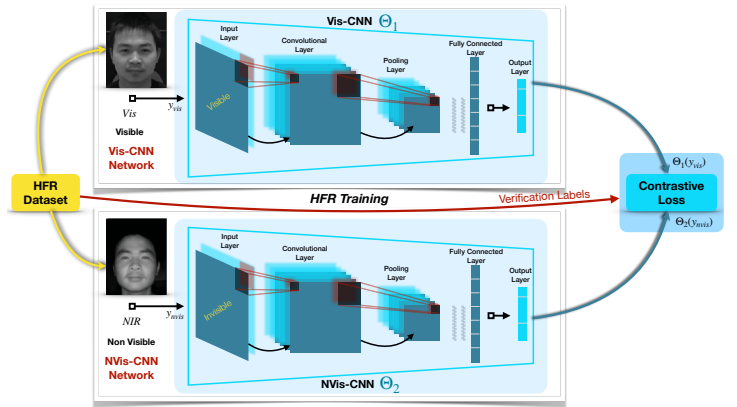


Fig. 9: **CNNs.** Flowchart depicting a two-branch convolutional neural network, learning domain-invariant feature representation.

Many existing techniques have been developed based on conditional GANs to address the CFR problem (see Figure 10). The generator takes a thermal image as input, seeking to produce a synthesized visible image as output. The discriminator is trained to distinguish between two pairs of images: the real pair, consisting of an input thermal image and a target visible image, and the synthesized pair, consisting of an input thermal image and a synthesized visible image [10], [13], [59], [61]. As noted in these works, there were notable differences in the use of architectures and loss functions. Some variants of architectures such as multi-scale generator [13] and multi-scale discriminator [11] were used in order to account for scale variance. There also exist variants of loss functions, including attribute loss [13], identity loss [10] and shape loss [70].

5.2.3 Loss Functions for cross-spectral face recognition

CNNs (Section 5.2.1) and GANs (Section 5.2.2) constitute fundamental deep learning networks. Once such network architectures are designed, suitable loss functions are chosen to minimize prediction errors. Therefore, one active direction in CFR has to do with the development of efficient *loss functions* [75]. Loss functions are pertinent in deep architectures, as they aim to measure how well algorithms

TABLE 3: **Loss Functions.** A comprehensive list of loss functions \mathcal{L} from traditional FR to CFR. Here, N is the number of samples, T is the number of samples in a mini-batch, W is the weight matrix, b is the bias term, x_i and y_i are the i^{th} training sample and the according class label, respectively. $\theta_{y_i} \in \left[\frac{k\pi}{m}, \frac{(k+1)\pi}{m} \right]$ with $k \in [0, m-1]$ and $m \geq 1$.

Task	Name	Notation	Reference	Function \mathcal{L}
FR	Softmax (Cross-Entropy)	\mathcal{L}_s	[71]	$-\frac{1}{N} \sum_{i=1}^N \log \left(\frac{e^{W_{y_i}^T x_i + b_{y_i}}}{\sum_{j=1}^n e^{W_j^T x_i + b_j}} \right)$
	Center Loss	\mathcal{L}_{ce}	[72]	$\frac{1}{2} \sum_{i=1}^N \ x_i - c_{y_i}\ _2^2$
	Marginal Loss	\mathcal{L}_{ma}	[73]	$\frac{1}{m^2 - m} \sum_{i,j,i \neq j}^m \left(\xi - y_{ij} \left(\theta - \frac{x_i}{\ x_i\ } - \frac{x_j}{\ x_j\ } \right) \right)$
	Angular Softmax Loss (SphereFace)	\mathcal{L}_{as}	[35]	$-\frac{1}{N} \sum_{i=1}^N \frac{e^{\ x_i\ \cos(m\theta_{y_i})}}{e^{\ x_i\ \cos(m\theta_{y_i})} + \sum_{j=1, j \neq y_i}^n e^{\ x_i\ \cos(\theta_j)}}$
	Large Margin Cosine Loss (CosFace)	\mathcal{L}_{co}	[74]	$-\frac{1}{N} \sum_{i=1}^N \log \left(\frac{e^{s(\cos(\theta_{y_i}) - m)}}{e^{s(\cos(\theta_{y_i}) - m)} + \sum_{j=1, j \neq y_i}^n e^{s \cos(\theta_j)}} \right)$
	Additive Angular Margin Loss (ArcFace)	\mathcal{L}_{aa}	[36]	$-\frac{1}{N} \sum_{i=1}^N \log \left(\frac{e^{s \cos(\theta_{y_i} + m)}}{e^{s \cos(\theta_{y_i} + m)} + \sum_{j=1, j \neq y_i}^n e^{s \cos(\theta_j)}} \right)$
CFR	Contrastive Loss	\mathcal{L}_{ct}	[44] - (12)	$\begin{cases} \frac{1}{2} \ f(x_i) - f(x_j)\ ^2, & \text{if } y_i = y_j \\ \frac{1}{2} \max(0, m - \ f(x_i) - f(x_j)\)^2, & \text{else.} \end{cases}$
	Triplet Loss	\mathcal{L}_{tp}	[47] - (13)	$\sum_{i=1}^N (\ f(x_i^a) - f(x_i^p)\ - \ f(x_i^a) - f(x_i^n)\ + m)$
	Tetrad Margin Loss	\mathcal{L}_{TML}	[54] - (15)	$\sum_{i \in \{N, V\}}^T \left(\frac{z_j^N \cdot z_j^V}{\ z_j^N\ \cdot \ z_j^V\ } - \frac{z_j^N \cdot z_l^V}{\ z_j^N\ \cdot \ z_l^V\ } + m_1 \right) + \sum_{i \in \{N, V\}}^T \left(\frac{z_j^N \cdot z_j^V}{\ z_j^N\ \cdot \ z_j^V\ } - \frac{z_j^V \cdot z_l^V}{\ z_j^V\ \cdot \ z_l^V\ } + m_2 \right)$

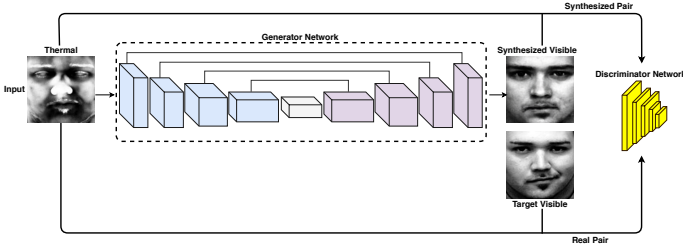


Fig. 10: **GANs.** Flowchart depicting a conditional generative adversarial network for synthesizing visible faces from conditional infrared (thermal) faces.

are able to perform correct predictions. In the CFR-context, the loss function is specifically designed to mitigate cross-spectral impact, in order to minimize intra-class variation and maximize inter-class variation [44], [47], [54].

Loss functions used in CFR are frequently adapted from traditional FR. We note that the predominantly used loss function in traditional FR remains to be *softmax*, which is targeted to maximize the probability that the same subject belongs to the target class. Therefore, it encourages the separability of features. *Center loss* [72] seeks to minimize distances between deep features and their corresponding class centers by simultaneously learning a center for individual classes. However, we note that center loss does not encourage separability of features. Therefore, it is common practice to perform a joint supervision of the softmax loss with center loss. Some other approaches combine euclidean margin-based losses with softmax loss to perform joint supervision. Recently, it has been shown that the features learned by softmax loss have an intrinsic angular distribution [35]. Since then, a flurry of angular-based loss functions

have been proposed to impose discriminative constraints on a hypersphere manifold [35], [36], [74]. We summarize loss functions in Table 3.

In most traditional FR systems, samples belonging to the same subject are treated without any differentiation. However, in CFR, samples are divided into different categories based on their spectrum information. This prompts the use of loss functions that can accept a pair of inputs [44], triplet of inputs [47], as well as quadruplet of inputs [54]. These loss functions have achieved impressive performance. Admittedly, directly using loss functions from traditional FR for CFR is based on the premise that facial appearance from other spectral bands is close to the visible spectral band. This is applicable in the case of comparing NIR against VIS faces. With increase in wavelength, difference in the facial appearance also starts to increase. Thus, adversarial loss functions used in GAN can be used to perform the synthesis.

5.3 Face Comparison

Trained CNNs or GANs for CFR produce deep feature representations for a given probe-image, which are then compared with those of the gallery images. Using the same notation introduced in Section 2, let $X^s = \{\mathbf{x}_i^s\}_{i=1}^n \subset \mathcal{X}^s$ and $X^t = \{\mathbf{x}_i^t\}_{i=1}^n \subset \mathcal{X}^t$ denote the set of samples from the *Source* (visible) and the *Target* (infrared) modalities, respectively. The corresponding shared set of labels are denoted by $Y = \{y_j\}_{j=1}^n \subset \mathcal{Y}$.

Suppose Θ denotes the deep process of extracting d features from a CNN, then the similarity score between two templates can be computed as a function \mathcal{S} referred to as the *measure of similarity* ranging between 0 and 1, where 1 represents a high similarity. As an example, the *cosine*

distance is widely used to calculate such similarity, for all k -index identities $\in [1, n]$:

$$\begin{aligned} \mathcal{S}(\mathbf{x}_k^s, \mathbf{x}_k^t) &= \cos(\mathbf{s}, \mathbf{t}) = \frac{\langle \mathbf{s}, \mathbf{t} \rangle}{\|\mathbf{s}\| \|\mathbf{t}\|} \\ &= \frac{\sum_{j=1}^d s_j t_j}{\sqrt{\sum_{j=1}^d (s_j)^2} \sqrt{\sum_{j=1}^d (t_j)^2}}, \end{aligned} \quad (11)$$

where, $\mathbf{s} = \Theta(\mathbf{x}_k^s)$ and $\mathbf{t} = \Theta(\mathbf{x}_k^t)$. Table 1 reports cosine similarity scores of state-of-the-art face matchers, when comparing thermal images depicted in Figure 6. Other Euclidean distance based measures such as L_2 and L_1 can also serve as similarity metrics.

ALGORITHMS OF DIFFERENT SPECTRA

FR operating on imagery beyond the visible spectrum can be categorized as *cross-spectrum featured-based algorithms* or *cross-spectrum images synthesis algorithms* (Figure 2). The former involve comparison of infrared probe against a gallery of visible face images, within a common feature subspace. However, after the success of image synthesis based on GANs, cross-spectrum images synthesis algorithms have attempted to synthesize a “pseudo-visible” image from an infrared image. Given the synthesized face image, both academic and commercial-off-the-shelf (COTS) FR-systems trained on visible spectrum, can be utilized for comparison. Furthermore, intensive research has been done to exploit the polarimetry thermal images to further improve CFR.

6 REFLECTIVE IR-TO-VISIBLE FR

6.1 Near Infrared

The appearance difference between NIR and VIS face images is less pronounced compared to other spectral bands and, hence, shared feature representations have often been proposed [44], [45], [46], [47], [68]. CNNs are suitable for NIR-to-VIS CFR scenario, since they seek to automatically extract representative face features. Nevertheless, a challenge remains, which has to do with the illumination-variation between the two modalities. We proceed to discuss a number of recent work, constituting prominent state-of-the-art approaches in matching NIR against VIS face images. These algorithms along with their individual loss functions are summarized in Figure 11. Further, we also list in Table 4 the NIR-to-VIS face comparison performances on public benchmark datasets.

TRIVET. Liu *et al.* [47] proposed a CNN with ordinal measures (o-CNN), pre-trained on visible images from the large-scale CASIA WebFace dataset [81] and hence is able to extract general face features, which has been fine-tuned on pairs of NIR-VIS face images, in order to learn a domain-invariant deep representation. To cope with limited image pairs, two types of NIR-VIS triplet loss functions were used, reducing intra-class variations by iteratively setting NIR and VIS images as anchors, such that the network focuses on the identity distinction instead of the spectrum classification.

IDNet. Reale *et al.* [44] utilized GoogLeNet networks with small convolutional filters, pre-trained on the visible CASIA WebFace dataset. For NIR-to-VIS CFR scenario, two

identical networks were initialized based on the pre-trained network by excluding fully connected and softmax layers. The outputs from these two networks, i.e., VisNet and NIR-Net, were concatenated to create a siamese network with contrastive loss. Such a coupled deep network design was able to map NIR and VIS faces into a spectrum-independent feature space.

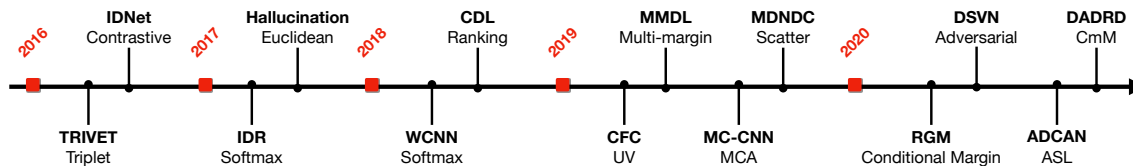
IDR. He *et al.* [45] presented a CNN-based approach targeted to map both NIR and VIS images into a common subspace by separating the feature space into a shared layer: NIR- and VIS-layer. While the shared layer encoded the modality-invariant identity information, the NIR- and VIS-layers encoded the modality-variant spectrum information, respectively. The NIR and VIS images were respectively input to the two CNN channels with shared parameters. Compared to similar CNN pipelines [44], [47], the proposed method jointly learned identity and spectrum information, leading to substantial performance gains on the CASIA NIR-VIS 2.0 dataset.

Hallucination. Lezama *et al.* [49] proposed an approach, which adapts a pre-trained VIS-CNN model towards generating discriminative features for both VIS and NIR face images, without retraining the network. Their approach consisted of two core components, cross-spectral hallucination and low-rank embedding, aiming at modifying both inputs and outputs of the CNN for CFR. Firstly, cross-spectral hallucination was used to transform the NIR image into the VIS spectrum by learning correspondences between NIR and VIS patches. Next, a low-rank embedding was used to restore a low-rank structure that simultaneously minimized the intra-class variations, while maximizing the inter-class variations. Three pre-trained VIS-CNN models, including VGG-S, VGG-face and COTS, were evaluated on the CASIA NIR-VIS 2.0 dataset.

WCNN. He *et al.* [46] proposed a novel method entitled *Wasserstein Convolutional Neural Network* (WCNN) streamlined to learn invariant features between NIR and VIS face images. Similar to their previous work [45], the proposed WCNN divided the high-level layer of the shared CNN into two orthogonal subspaces that contain modality-invariant identity features and modality-variant spectrum features. In addition, Wasserstein distance was used to measure the difference between heterogeneous feature distributions to reduce the modality gap. We note that their work represented the first attempt to formulate a probability-based distribution learning for VIS-to-NIR face comparison. WCNN outperformed the work of He *et al.* [45], improving the performance on the CASIA NIR-VIS 2.0 dataset.

CDL. Wu *et al.* [68] designed a *Coupled Deep Learning* (CDL) approach, identifying a shared feature space, in order to reduce modality differences in heterogeneous face comparison. The loss function of CDL consisted of two different components: (a) relevance constraints that imposed a trace norm to the softmax loss and a block-diagonal prior to the fully connected layer; and (b) cross-modal ranking that employed triplet ranking regularization to enlarge the size of training data. A semi-hard triplet selection method was also adopted to further improve the NIR-to-VIS comparison performance. Both relevance and ranking losses were jointly optimized.

CFC. He *et al.* [12] proposed a GAN, termed *Cross-spectral*

Fig. 11: **Timeline of algorithm development.** NIR-to-VIS FR with their corresponding loss functions.TABLE 4: Rank-1 Accuracy and Verification Rate on different datasets for the **NIR-VIS** face comparison.

Year	Authors	Method	Loss	Dataset	Performance		
					Rank-1	FAR 1%	FAR 0.1%
2016	Liu <i>et al.</i> [47]	TRIVET	Triplet	CASIA NIR-VIS 2.0 [41]	95.74	98.1	91.03
				Oulu-CASIA NIR-VIS [76]	92.2	67.9	33.6
				BUAA-VisNir face [77]	93.9	93.0	80.9
	Reale <i>et al.</i> [44]	IDNet	Contrastive	CASIA NIR-VIS 2.0 [41]	87.1	-	74.5
				CASIA HFB [78]	97.58	96.9	85.0
2017	He <i>et al.</i> [45]	IDR	Softmax	CASIA NIR-VIS 2.0 [41]	97.3	98.9	95.7
				Oulu-CASIA NIR-VIS [76]	94.3	73.4	46.2
				BUAA-VisNir face [77]	94.3	93.4	84.7
Lezama <i>et al.</i> [49]	Hallucination	Euclidean	CASIA NIR-VIS 2.0 [41]	96.41	-	-	
2018	He <i>et al.</i> [46]	WCNN	Softmax	CASIA NIR-VIS 2.0 [41]	98.7	99.5	98.4
				Oulu-CASIA NIR-VIS [76]	98.0	81.5	54.6
				BUAA-VisNir face [77]	97.4	96.0	91.9
	Wu <i>et al.</i> [68]	CDL	Ranking	CASIA NIR-VIS 2.0 [41]	98.6	-	98.32
				Oulu-CASIA NIR-VIS [76]	94.3	81.6	53.9
			BUAA-VisNir face [77]	96.9	95.9	90.1	
2019	He <i>et al.</i> [12]	CFC (GAN)	UV	CASIA NIR-VIS 2.0 [41]	98.6	99.2	97.3
				Oulu-CASIA NIR-VIS [76]	99.9	98.1	90.7
				BUAA-VisNir face [77]	99.7	98.7	97.8
	Cao <i>et al.</i> [54]	MMDL	Multi-margin	CASIA NIR-VIS 2.0 [41]	99.9	-	99.4
				Oulu-CASIA NIR-VIS [76]	100.0	-	97.2
	Deng <i>et al.</i> [55]	MC-CNN	MCA	CASIA NIR-VIS 2.0 [41]	99.22	-	99.27
	Hu <i>et al.</i> [63]	MDNDC	Scatter	CASIA NIR-VIS 2.0 [41]	98.9	99.6	97.6
				Oulu-CASIA NIR-VIS [76]	99.8	88.1	65.3
2020	Cho <i>et al.</i> [56]	RGM	Conditional-margin	CASIA NIR-VIS 2.0 [41]	99.3	99.51	99.02
				BUAA-VisNir face [77]	99.67	99.22	-
	Hu <i>et al.</i> [79]	DSVN	Adversarial	CASIA NIR-VIS 2.0 [41]	99.0	99.7	98.6
				Oulu-CASIA NIR-VIS [76]	100.0	99.3	95.5
	Iranmanesh <i>et al.</i> [66]	CpGAN	Contrastive+Coupled +GAN+Eucl.+Perceptual	CASIA NIR-VIS 2.0 [41]	96.63	-	87.05
				CASIA HFB [78]	99.64	98.4	89.7
				CASIA NIR-VIS 2.0 [41]	99.1	99.6	98.5
	Hu <i>et al.</i> [64]	ADCANs	ASL	Oulu-CASIA NIR-VIS [76]	99.8	93.2	78.9
				BUAA-VisNir face [77]	99.8	99.7	98.4
				CASIA NIR-VIS 2.0 [41]	99.1	99.6	98.6
	Hu <i>et al.</i> [80]	DADRDR	CmM	Oulu-CASIA NIR-VIS [76]	100.0	98.5	92.9
				BUAA-VisNir face [77]	99.9	99.9	99.8

Face Completion (CFC), to synthesize VIS images from NIR images. The heterogeneous face synthesis process was divided into two complementary components: (a) a texture inpainting component that aims to recover a VIS facial texture map from a given NIR image; and (b) a pose correction component that aims to map any pose in NIR images to the frontal pose in VIS images. A warping procedure was used to fuse these two components in the adversarial network, which was regularized by the combinations of UV loss, adversarial loss and L1 reconstruction loss. In summary, the main contributions of this work had to do with creating a novel GAN-based end-to-end deep framework for cross spectral face synthesis without assembling multiple image patches. It contained encoder-decoder structured generators and two novel discriminators to fully consider variations of NIR and VIS images. This was the first time that unsupervised heterogeneous face synthesis problem was simplified to a one-to-one image translation problem. The decomposition of texture inpainting and pose correction enables the

generation of realistic identity preserving VIS face images possible.

MMDL. Cao *et al.* [54] combined heterogeneous representation network and decorrelation representation learning in order to design a *Multi-Margin based Decorrelation Learning* (MMDL) framework to extract decorrelated features for both VIS and NIR images. First, the heterogeneous representation network was initialized from a VIS face model and fine-tuned on both VIS and NIR face images. Second, a decorrelation layer was appended to shared feature layer of the representation network to extract decorrelated features for both VIS and NIR images.

MC-CNN. Deng *et al.* [55] proposed a *Mutual Component Convolutional Neural Network* (MC-CNN) to extract modality-invariant features. The novelty of MC-CNN was the incorporation of a generative module, i.e., the mutual component analysis (MCA), into the CNN by replacing the fully connected layer with MCA. VIS-NIR image pairs from the same subjects were first input to a shared CNN to

extract common feature vectors. Subsequently, these feature vectors were fed into the MCA layer. Finally, MCA loss was included as an additional regularization to the softmax loss.

MDNDC. Hu *et al.* [63] proposed *Multiple Deep Networks with scatter loss and Diversity Combination* (MDNDC). They used three ResNet-v1 networks; one being dedicated to feature extraction, in order to build the architecture of Multiple Deep Networks (MDN), followed by the two other networks in parallel. Jointly with the MDN, a Scatter loss (SL) [82] was used as a loss function, which attempts to maximize distance between the classes and minimize distance within the class to learn highly discriminative features for the CFR task. In addition to the MDN, a joint decision strategy named Diversity Combination (DN) was introduced to auto-adjust weights of all three deep networks of the MDN and make a joint classification decision.

RGM. Cho *et al.* [56] were interested in Relational Deep Feature Learning for CFR. Therefore, to bridge the domain gap between visible and invisible spectrum, they proposed a *Relational Graph-structured Module* (RGM) focused on facial relational information. Their graph RGM performed relational modeling from node vectors that represent facial components such as lips, nose and chin. They also performed recalibration by considering global node correlation via *Node Attention Unit* (NAU) to focus on the more informative nodes arising from the relation-based propagation. Furthermore, they suggested a novel conditional-margin loss function *C-Softmax* for efficient projection learning on the common latent space of the embedding vector that adaptively uses the inter-class margin.

DSVN. Hu *et al.* [79] proposed *Disentangled Spectrum Variations Networks* (DSVN) to disentangle spectrum variations between VIS and NIR domains and to separate the modality-invariant identity information from modality-variant spectrum information. DSVN is comprised of two major components: spectrum-adversarial discriminative feature learning (SaDFL) and step-wise spectrum orthogonal decomposition (SSOD). The SaDFL was further divided into identity-discriminative subnetwork (IDNet) and auxiliary spectrum adversarial subnetwork (ASANet). The IDNet was used to extract identity discriminative features. The ASANet, on the other hand, was used to eliminate modality-variant spectrum information. Both IDNet and ASANet were designed to extract domain-invariant feature representations via adversarial learning.

ADCANs. Hu *et al.* [64] proposed an effective *Adversarial Disentanglement spectrum variations and Cross-modality Attention Networks* (ADCANs) for the VIS-to-NIR CFR scenario. To reduce the gap of cross-modal images and solve the NIR-VIS CFR problem, the authors set-up three key components which are able to learn identity-related and modality-unrelated features. Firstly, they proposed a new objective loss termed *Advanced Scatter Loss* (ASL), aiming at capturing within- and between-class information of the data and embedding them in the network for more effective training, focusing on categories with small inter-class distance and increasing the distance between them. Then, a *Modality-adversarial Feature Learning* (MaFL) including an Identity-Discriminative Feature Learning Network (IDFLN) and a Modality-Adversarial Disentanglement Network (MADN) were incorporated to improve the feature representation of

the identity-discriminative component as well as to highlight the spectrum variations through adversarial learning. Finally, a *Cross-modality Attention Block* (CmAB) was introduced, in order to guide the network in selecting pertinent features and suppress noise information. CmAB sequentially applies spatial and channel attention modules to both, IDFLN and MADN, in order to increase the representation ability between them.

DADR. Hu *et al.* [80] proposed the *Dual Adversarial Disentanglement and deep Representation Decorrelation* (DADR) approach to reduce the gap between NIR-VIS modalities, while enhancing the learning of identity-related features. At the same time, DADR sought to effectively disentangles the additional residual-related features (i.e. PIE) rather than only extracting modality-related (i.e. NIR and VIS) and identity-related features. In contrast with their prior work, MDNDC [63] and ADCAN [64], the DADR method combined three key components. Firstly, they proposed a new objective loss termed *Cross-modal Margin* (CmM), and attempted to enhance the learning identity-related features, which captures within- and between-class information of the data (i.e., occlusion, pose, distance, lighting and expressions), while also reducing the modality gap by using a center-variation item. Then, they introduced a *Mixed Facial Representation* (MFR) which is divided into three layers: “(I) Identity-related layer”, “(M) Modality-related layer” and “(R) Residual-related layer”. A *Dual Adversarial Disentanglement Variation* (DADV) was then designed to reduce the intra-class variation with the help of adversarial learning, including both *Adversarial Disentangled Modality Variations* (ADMV) and *Adversarial Disentangled Residual Variations* (ADRV). These adversarial mechanisms disentangle the spectrum variation (in terms of data heterogeneity) and eliminate residual variations such as PIE, respectively. Finally, a *Deep Representation Decorrelation* (DRD) was embedded to the three MFR layers of DADV for the purpose of making them unrelated to each other and enhance feature representations. The DADR method, combining CmM, DADV and DRD into a unified framework, is depicted in Figure 12.

DVG-Face. Fu *et al.* [83] proposed a novel Dual Variational Generation (DVG-Face) framework to learn the joint distribution of paired heterogeneous images. Identity information from large-scale visible face data was also utilized to tackle the problem of identity diversity sampling induced by the small-scale paired heterogeneous data. To ensure identity consistency, a pairwise identity preserving loss was applied to generated paired heterogeneous images. A contrastive learning scheme was employed to train the heterogeneous face matching with positive pairs from generated paired heterogeneous images and negative pairs from different identity samplings. The proposed DVG-Face was an extension from the authors’ previous work DVG [84] that greatly improved the identity diversity of generated face images.

Summary of NIR-to-VIS Face Comparison

Comparing face images in NIR against VIS can be coarsely classified into (a) cross-spectrum featured-based methods [44], [45], [46], [47], [54], [55], [56], [68], [79] and (b) cross-spectrum image-synthesis methods [12], [49]. Existing

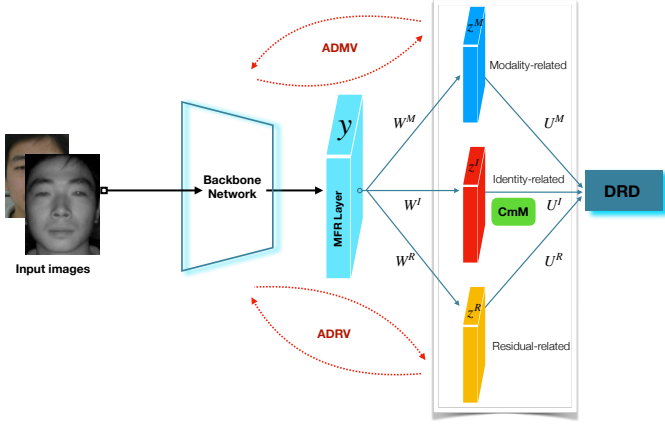


Fig. 12: **Overview of the DADRD [80] model:** learn identity-discriminative features and disentangle within-class variations. DADRD combines three key components, including *CmM* loss, *DADV* consisting of both *ADMV* and *ADRV* and *DRD* embedded into the three previous *MFR* layers.

methods (a) predominantly seek to learn a domain-invariant deep representation between NIR and VIS samples, which is motivated by the presence of some similar textures observed in NIR as well as VIS-domains. Such approaches can incorporate two different ways to construct the inputs of the networks. Firstly, NIR and VIS images pertaining to same subjects are related in positive pairs [44], [45], [46], [54], [55], [79], constituting two identical subnetworks with shared weights. A *contrastive loss* in this context minimizes the intra-class distance

$$\mathcal{L}_{ct} = \begin{cases} \frac{1}{2} \|f(x_i) - f(x_j)\|^2, & \text{if } y_i = y_j \\ \frac{1}{2} \max(0, m - \|f(x_i) - f(x_j)\|)^2, & \text{else.} \end{cases} \quad (12)$$

Secondly, a triplet can be formed, where a NIR image is set as an anchor, a VIS image of the same subject as a positive sample, and an additional VIS image pertaining to a different subject as a negative sample. Alternatively, a triplet can be formed by setting a VIS image as an anchor and using NIR images from the same and different subjects as positive and negative samples, respectively [47], [68]. This leads to three identical subnetworks with shared weights, where the *triplet loss* is defined as

$$\mathcal{L}_{tp} = \sum_i^N (\|f(x_i^a) - f(x_i^p)\| - \|f(x_i^a) - f(x_i^n)\| + m). \quad (13)$$

Here, x_i^a is an anchor image, x_i^p is a positive sample and x_i^n is a negative sample. The goal of triplet loss is to ‘push’ the negative sample x_i^n away from the anchor x_i^a by a margin m compared to the positive sample:

$$\|x_i^a - x_i^p\|^2 + m \leq \|x_i^a - x_i^n\|. \quad (14)$$

The triplet loss attempts to minimize the intra-class distance, while maximizing the inter-class distance. Unlike triplet, where a group of three samples is selected, the *Tetrad Margin Loss* (TML) [54] uses a group of four samples to construct tetrad tuples. The designed tetrad sample selection strategy was to choose four heterogeneous decorrelation representations, viz., $\{z_j^N, z_j^V, z_k^N, z_l^V\}$. Herein, $\{z_j^N, z_j^V\}$ are samples

from the same identity, z_k^N denotes the closest NIR sample to z_j^V from another identity, z_l^V represents the closest VIS sample to z_j^N from another identity. The tetrad margin loss is defined as:

$$\begin{aligned} \mathcal{L}_{TML}(z_j^N, z_j^V, z_l^V) = & \sum_{i \in \{N, V\}}^T \left(\frac{z_j^N \cdot z_j^V}{\|z_j^N\| \cdot \|z_j^V\|} - \frac{z_j^N \cdot z_l^V}{\|z_j^N\| \cdot \|z_l^V\|} + m_1 \right) \\ & + \sum_{i \in \{N, V\}}^T \left(\frac{z_j^N \cdot z_j^V}{\|z_j^N\| \cdot \|z_j^V\|} - \frac{z_j^V \cdot z_l^V}{\|z_j^V\| \cdot \|z_l^V\|} + m_2 \right). \end{aligned} \quad (15)$$

Subsequently, $\mathcal{L}_{TML}(z_j^N, z_j^V, z_k^N, z_l^V)$ can be defined as

$$\begin{aligned} \mathcal{L}_{TML}(z_j^N, z_j^V, z_k^N, z_l^V) = & \mathcal{L}_{TML}(z_j^N, z_j^V, z_l^V) \\ & + \mathcal{L}_{TML}(z_j^V, z_j^N, z_k^N). \end{aligned} \quad (16)$$

T represents the number of samples in a mini-batch, while m_1 and m_2 are the two margins. The tetrad margin loss can be regarded as the combination of two triplet losses [47], [68]. Intuitively, $\mathcal{L}_{TML}(z_j^N, z_j^V, z_l^V)$ is very similar to assigning a NIR image z_j^N as an anchor, a VIS image z_j^V of the same subject as a positive sample, and another VIS image z_l^V of a different subject as a negative sample. The difference lies in the use of cosine distance other than the euclidean distance to compare the similarity. Both triplet loss and tetrad margin loss use the hard-sample mining strategy.

In addition to the contrastive loss, triplet loss and tetrad margin loss, other loss functions have notably been proposed in the NIR-to-VIS literature. In [45], a variant of *softmax loss* was proposed in order to learn modality invariant subspace. The softmax loss function is defined as:

$$\begin{aligned} \mathcal{L} = & \sum_{i \in \{N, V\}} \text{softmax}(F_i, c, \Theta, W, P_i) \\ = & - \sum_{i \in \{N, V\}} \left(\sum_{j=1}^N \log(\hat{p}_{ij}) \mathbb{1}_{\{y_{ij}=c\}} \right), \quad (17) \\ \text{s.t. } & P_i^T W = 0, \quad i \in \{N, V\}, \end{aligned}$$

where, F_i is the fully connected layer of WCNN, c is the class label and Θ is the set of WCNN parameters. W is used to denote the weight matrix of the modality-invariant features (i.e., shared features across spectral domain) and P_i denotes the weight matrix of the spectrum-specific features (i.e., features which are spectral dependent). $\mathbb{1}$ is an indicator function and p_{ij} denotes the predicted class probability. $P_i^T W$ corresponds to an orthogonal constraint imposed to make the features uncorrelated.

6.2 Shortwave Infrared

To date, SWIR-to-visible has received limited attention. This is reflected in the scarcity of deep models and in the lack of publicly available SWIR face datasets (see Table 8). We proceed to summarize existing prominent handcrafted methods [7], [85].

pre-CNN. Research of Bourlai *et al.* [86] firstly investigated face verification related to the SWIR band. The authors introduced a *geometric* and *photometric normalization* (PN) scheme in order to compensate for the variable environment, coupled with *contrast limited adaptive histogram*

equalization (CLAHE). Based on that, three FR methods (commercial and academic) were tested using the *West Virginia University* (WVU) Multi-spectral database.

Kalka *et al.* [87] extended the previous work w.r.t. pre-processing [86] by adding *single scale retinex* (SSR) and also explored the cross-photometric score level fusion rule. For the experiment, three datasets were considered including different environmental setup (fully controlled/semi controlled/uncontrolled). Their finding provided insights such as that pre-processing with PN improved FR performance, obtaining highest results up to Rank-1 accuracy of 100%, when images were acquired under fully controlled conditions.

Bourlai *et al.* [85] pursued the intra-spectral and cross-spectral FR specially focused on (NIR/SWIR/MWIR)-imaging at various standoff distances and different environmental conditions. They merged previous work [86], [87] in order to demonstrate that jointly, the use of independent or combined PN, CLAHE, SSR and cross-photometric score level fusion rule were able to reach better results under different environmental setups.

CMLD. Cao *et al.* [88] proposed a local operator called *Composite Multilobe Descriptors* (CMLD) with the aim to extract facial feature through all IR-spectral bands. This operator combined Gaussian function, Local binary patterns (LBP), Weber local descriptor and histogram of oriented gradients (HOG). The experimental results showed that for the SWIR-to-visible scenario, CMLD performed on a private dataset containing SWIR images (at various standoff distances), a Rank-1 accuracy of 78.7% and a verification rate of 99.5% at FAR 10%. Authors also used CMLD to conduct a study on cross-spectral *partial* FR in order to understand the face area which contained useful information for CFR. They found that the eye region is most informative for FR beyond the visible.

VGGFace. Bihn *et al.* [50] examined the ability of using pretrained VGG-Face network on visible images to extract features on SWIR images. Hypothesized was that the VGG-Face network would perform well on face images taken from both, VIS and SWIR wavelengths since their facial appearance difference is not as significant as these images captured at MWIR and LWIR wavelengths. SWIR wavelengths at 935 nm, 1060 nm, 1300 nm, 1550 nm were evaluated, as well as a composite image formed by combining 1060 nm, 1300 nm, and 1550 nm. Deep features extracted from the *fc7* layer of VGGFace network were used, resulting in a 4096-dimensional feature vector. Euclidean distance calculated between feature representations of VIS and SWIR images was used as a similarity comparison.

7 EMISSIVE IR-TO-VISIBLE FR

7.1 Midwave Infrared

Appearance difference between MWIR and VIS is more pronounced than NIR and SWIR (Figure 4). Therefore, learning a common feature subspace for MWIR-to-VIS is a challenging problem. In most cases, methods developed over the years have relied on GANs to synthesize visible face images from thermal face images. Illustrative examples are shown in Figure 13 and 15. We report the related MWIR-to-VIS face comparison performance in Table 5.

DPM. One of the first successful MWIR-to-VIS approaches with deep neural network was introduced by Sarfraz *et al.* [89], termed *Deep Perceptual Mapping* (DPM). Their approach was targeted to learn a non-linear mapping between visible and thermal domains (including MWIR and LWIR) while preserving the identity information. Specifically, a feed forward neural network was constructed to regress densely computed features from the visible image to the corresponding thermal image. A MSE loss function was used to measure the perceptual difference between the visible and thermal images. Further, a regularization term with Frobenius norm of the projection matrix was also introduced.

TV-GAN. Zhang *et al.* [59] proposed a *Thermal-to-Visible Generative Adversarial Network* (TV-GAN) that can synthesize visible images from their corresponding thermal images while maintaining identity information during the reconstruction. To preserve the identity information, a multi-task discriminator was designed. This discriminator served two different purposes. Firstly, one output of this discriminator was used to differentiate whether the generated samples were "real" or "fake". Secondly, the other output of this discriminator was used to perform identity classification in the context of supervised learning, given that the label identities are provided. Note that this identity classification was regarded as a closed-set FR. That means the identity associated with a given sample had already been seen in the training dataset. The proposed TV-GAN is similar to the auxiliary classifier GAN (or AC-GAN). Experiments were conducted on IRIS dataset [91] and compared against three baselines approaches. TV-GAN against other GAN-methods are visualized in Figure 15.

SG-GAN. Chen *et al.* [10] proposed the use of *Semantic-Guided Generative Adversarial Network* (SG-GAN) to automatically synthesize visible face images from their thermal counterparts. Specifically, semantic labels, extracted by a face parsing network were used to compute a semantic loss function to regularize the adversarial network during training. These semantic cues denoted high-level facial component information associated with each pixel. Further, an identity extraction network was leveraged to generate multi-scale features to compute an identity loss function. To achieve photo-realistic results, a perceptual loss function was introduced during network training to ensure that the synthesized visible face was perceptually similar to the target visible face image. Experiments involving PCSO [92] face dataset showed that the proposed method achieved promising results in both face synthesis and CFR (see Figure 13).

Summary of MWIR-to-VIS Face Comparison

MWIR-to-VIS CFR scenario has been scarcely studied in scientific literature. Partly this is the case due to lack of public benchmark datasets. Interestingly, early research on comparing MWIR-to-VIS face images adopted a neural network [89], formulated by sequential operations of fully connected layer and non-activation layer. This simple feed-forward neural network does not involve the use of convolution units and can be represented as

$$H(x) = h^N = g(W^N h^{N-1} + b^N), \quad (18)$$

TABLE 5: Rank-1 Accuracy and Verification Rate on different dataset for the MWIR-VIS face comparison.

Year	Authors	Methods	Dataset	Performance %
2017	Sarfraz <i>et al.</i> [89]	DPM	NVESD [90]	98.66 @Rank-1
2018	Zhang <i>et al.</i> [59]	TV-GAN	IRIS [91]	19.90 @Rank-1
2019	Chen <i>et al.</i> [10]	SG-GAN	PCSO [92]	92.16 @AUC - 15.01 @EER
2020	Iranmanesh <i>et al.</i> [66]	CpGAN	NVESD [90]	96.10 @Rank-1
			WSRI [93]	97.80 @Rank-1
2021	Neehar <i>et al.</i> [94]	Pix2Pix-ATC	MILAB-VTF(B) [94]	59.3 @AUC - 43.4 @EER
		CycleGAN-ATC	MILAB-VTF(B) [94]	54.9 @AUC - 46.4 @EER
		CUT-ATC	MILAB-VTF(B) [94]	68.8 @AUC - 36.3 @EER

where, W is the projection matrix, h is the hidden layer and b is the bias. Basically, the output of current hidden layer is a multiplication of project matrix with the output of previous hidden layer. g is a non-activation function to ensure that the mapping is non-linear. The objective function of DPM was formulated as

$$\arg \min_{W,b} \mathcal{L} = \frac{1}{M} \sum_{i=1}^M (\bar{x}_i - t_i)^2 + \frac{\lambda}{N} \sum_{i=1}^N (\|W^k\|_F^2 + \|b^k\|_2^2). \quad (19)$$

Here, the first term is the mean square error between the feature vectors of visible \bar{x}_i and thermal t_i image. The second term serves as a regularizer on the weight matrix W and bias b . Although the DPM showed promising results on comparing SWIR against VIS images, the performance was still far from satisfactory.

Recent developments of neural networks, specifically in GANs, have pushed the frontiers of SWIR-to-VIS CFR scenario. Both TV-GAN [59] and SG-GAN [10] are inspired by Pix2Pix [95], which involves the use of adversarial loss and \mathcal{L}_1 loss to regularize the image synthesis process. The \mathcal{L}_1 loss was used to measure the per-pixel difference between synthesized visible face image and target visible face image. Compared to Pix2Pix, TV-GAN modified the output of the discriminator to perform a closed-set identification. Therefore, a new identity loss was introduced in TV-GAN. SG-GAN, on the other hand, adds more loss functions to the Pix2Pix, including perceptual loss, identity loss and semantic loss. An ablation study was used to demonstrate the individual functionalities of the loss functions (see Figure 13).

7.2 Longwave Infrared

Face images captured under MWIR and LWIR tend to look very similar (Figure 4). Therefore, algorithms developed to address LWIR-to-VIS closely resembles that of MWIR-to-VIS. Most developed algorithms for LWIR-to-VIS CFR scenario were based on GANs. Here, we give a brief summary of recent representative works for LWIR-to-VIS comparison, related performance are reported in Table 6 and we illustrate the timeline of developments in Figure 14.

Landmark-based CycleGAN. Wang *et al.* [70] proposed a detection network to extract facial landmarks from visible faces and use that to guide the generative network to preserve geometric shapes. Their network was based on CycleGAN [100], targeted to perform translation between the thermal and visible face images. The detection network extracted 68-landmarks from visible faces, constructing the

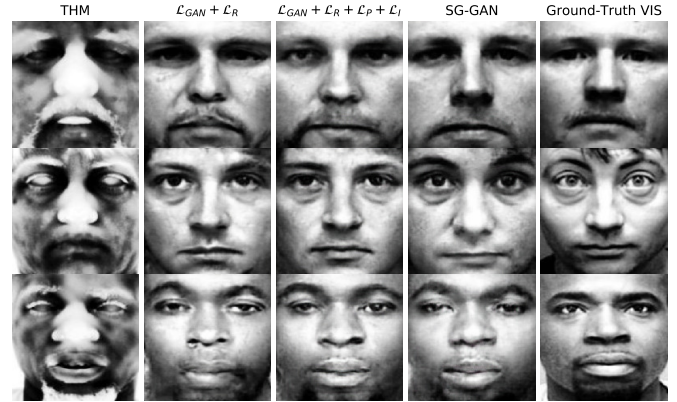


Fig. 13: **Synthesizing VIS face images** from THM images on the PCSO dataset. Compared to the use of the “ $\mathcal{L}_{GAN} + \mathcal{L}_R + \mathcal{L}_P + \mathcal{L}_I$ ” loss function, the output of SG-GAN is semantically more close to the ground-truth VIS image especially around the salient facial regions.

shape loss function. To perform the experiment, they established a new database (available online), including 33 subjects with 792 thermal-visible pair images.

DCA. Kantarcı *et al.* [60] presented a *Deep Convolutional Autoencoder* (DCA), specifically based on the *U-Net* [57] architecture, including Up Convolution and Difference of Gaussians (DoG), which was modified for the purpose to learn the non-linear mapping between visible and thermal face images for CFR. In the meantime, they showed that applying preprocessing and alignment would help to close the gap between these two domains and was able to improve the performance further. The proposed approach was extensively tested on three publicly available thermal-visible datasets: Carl [97], UND-X1 [96] and EURECOM [102]. In addition, authors have manually annotated 6 facial landmarks on the Carl and EURECOM datasets in order to align the faces and assess alignment’s impact on the performance (we observe that alignment increased the performance by around 2%). They conduct experiments with three different setups: the first two experiments investigated the effect of the decoder method, DoG filter were not applied to images as preprocessing step. For the third experiment, the effect of the DoG filter was tested on the Up Convolutional Autoencoder Model, proposed in this work.

CRN. Mallat *et al.* [103] proposed a solution based on *Cascaded Refinement Network* (CRN). Their approach did not require a large amount of training data, owing to a limited number of training parameters. CRN is a type of CNN that consists of inter-connected refinement modules,

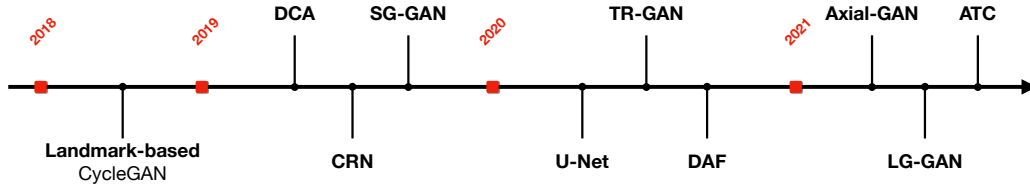


Fig. 14: Timeline of developments in algorithms: LWIR-to-VIS face recognition.

TABLE 6: Rank-1 Accuracy and Verification Rate on different dataset for the LWIR-VIS face Comparison.

Year	Authors	Methods	Dataset	Performance %
2017	Sarfranz <i>et al.</i> [89]	DPM	UND X1 [96]	83.73 @Rank-1
			Carl [97]	71.00 @Rank-1
			NVESD [90]	97.33 @Rank-1
	Zhang <i>et al.</i> [98]	GAN-VFS	Polarimetric thermal [42] - <i>Therm. Probe</i>	84.00 @Rank-1
			Polarimetric thermal [42] - <i>Therm. Probe</i>	85.61 @Rank-1 - 79.30 @AUC - 27.34 @EER
		ARL-VTF [99]	97.94 @AUC - 08.14 @EER	
2018	Wang <i>et al.</i> [70]	CycleGAN [100]	private database	88.90 @Rank-1 - 98.80 @Rank-3 - 99.80 @Rank-5
		CycleGAN-Based	private database	91.60 @Rank-1 - 99.30 @Rank-3 - 99.90 @Rank-5
	Iranmanesh <i>et al.</i> [101]	CpDCNN	Polarimetric thermal [42] - <i>Therm. Probe</i>	88.57 @Rank-1
	Di <i>et al.</i> [61]	AP-GAN	Polarimetric thermal [42] - <i>Therm. Probe</i>	84.16 @AUC - 23.90 @EER
2019	Kantarci <i>et al.</i> [60]	DCA	UND X1 [96]	87.20 @Rank-1
			EURECOM [102]	88.33 @Rank-1
			Carl [97]	85.00 @Rank-1
	Mallat <i>et al.</i> [103]	CRN	EURECOM [102]	82.00 @LightCNN
	Iranmanesh <i>et al.</i> [104]	AGC-GAN	Polarimetric thermal [42] - <i>Therm. Probe</i>	89.25 @Rank-1
	Di <i>et al.</i> [105]	SAGAN	Polarimetric thermal [42] - <i>Therm. Probe</i>	91.49 @AUC - 15.45 @EER
Chen <i>et al.</i> [10]	SG-GAN	ARL-VTF [99]	99.28 @AUC - 03.97 @EER	
		Polarimetric thermal [42] - <i>Therm. Probe</i>	93.08 @AUC - 14.24 @EER	
2020	Chatterjee <i>et al.</i> [58]	U-Net	Nagoya University	69.60 @Rank-1
	Kezebou <i>et al.</i> [51]	TR-GAN	TUFTS [9]	80.70 @Resnet50 - 88.65 @VGG16
	Iranmanesh <i>et al.</i> [66]	CpGAN	UND X1 [96]	76.40 @Rank-1
			NVESD [90]	93.90 @Rank-1
			Polarimetric thermal [42] - <i>Therm. Probe</i>	89.05 @Rank-1
	Di <i>et al.</i> [13]	Multi-AP-GAN	Polarimetric thermal [42] - <i>Therm. Probe</i>	90.99 @AUC - 17.81 @EER
	Fondje <i>et al.</i> [106]	DAF	Polarimetric thermal [42] - <i>ext. - Therm. Probe</i>	94.20 @Rank-1
ARL-VTF [99]			99.76 @AUC - 2.30 @EER	
2021	Immisisetti <i>et al.</i> [107]	Axial-GAN	ARL-VTF [99]	94.4 @AUC - 12.38 @EER
	Anghelone <i>et al.</i> [108]	LG-GAN	Polarimetric thermal [42] - <i>Therm. Probe</i>	93.99 @AUC - 13.02 @EER
			ARL-VTF [99]	96.96 @AUC - 5.94 @EER
	Neehar <i>et al.</i> [94]	Pix2Pix-ATC	ARL-VTF [99]	91.3 @AUC - 16 @EER
			CycleGAN-ATC	96.8 @AUC - 9.2 @EER
		CUT-ATC	ARL-VTF [99]	97.7 @AUC - 6.9 @EER
TUFT [9]			87.4 @AUC - 21.3 @EER	

which gradually process the image synthesis from lowest resolution (4×4) to the highest resolution (128×128). The refine module includes three different layers, namely input, intermediate and output layers. A contextual loss function was used to train the CRN. The motivation to choose the contextual loss was based on two conditions: (a) robustness to roughly aligned THM-VIS pairs; and (b) invariant to outlier at the pixel level in the context of per-pixel loss. FR experiments on the EURECOM [102] dataset showed that the proposed method achieves better performance than TV-GAN. In addition, they performed CFR using their synthesized faces (facial variation = Neutral) with two systems, namely *OpenFace* and *LightCNN*.

U-Net. Chatterjee and Chu [58] presented a U-Net architecture with a residual network backbone to generate visible face images from thermal face images. The U-Net was modified by using residual blocks with skip-connections instead of the normal convolutional layers as the basic building components. Further, a pixel shuffle upsampling was introduced to replace the transposed convolution layers in the decoder part. A weighted combinations of two differ-

ent loss functions was used to train the proposed network, namely mean squared loss and perceptual loss. The proposed method was evaluated on thermal face dataset from *Nagoya University*, which contained 900 thermal images and 900 visible images captured simultaneously. A Rank-1 accuracy of 69.60% was achieved.

TR-GAN. Kezebou *et al.* [51] proposed a *Thermal to RGB Generative Adversarial Network* (TR-GAN) to automatically synthesize visible face images captured in the thermal domain. The TR-GAN employed an architecture similar to U-Net with cascade residual blocks for the generator. Basically, it replaced the Resnet blocks in the CycleGAN with cascaded-in- cascaded residual blocks. This ensured that the generator synthesizes images with consistent global and local structural information. For the discriminator, the TR-GAN used the same discriminator network architecture as CycleGAN. A pretrained VGG-Face recognition model was used to perform the face comparison after the thermal to visible image translation. The experiments were conducted on TUFTS face dataset and compared against TV-GAN, Pix2PixHD and CycleGAN. Figure 15 shows samples of

synthesized images performed by named models. In comparison, TR-GAN demonstrated superior performance in generating realistic images.

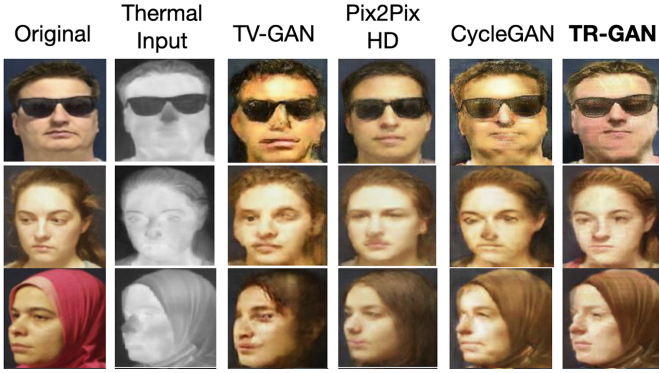


Fig. 15: **Synthesizing VIS face images** from thermal images on the TUFTS dataset [9] with different visualization results: **TR-GAN** [51], CycleGAN [11] and TV-GAN [59]. Figure credit: Kezebou *et al.* [51]

DAF. Fondje *et al.* [106] proposed a *Domain Adaptation Framework* (DAF) with a new feature mapping sub-network including (a) a *cross-domain identification-loss* function for effective “co-registration” and “synchronization” and (b) a *domain invariance-loss* function for cross-domain regularization. Within each domain, the feature representations have been acquired using a truncated pre-trained CNNs (based on VGG16 or ResNet50). Indeed, authors were interested to find the optimal depth level of the network while preserving the meaningful discriminative information shared by both visible and thermal spectrum. DAF is then embedded with their proposed *Residual Spectral Transform* (RST), which is a residual block. The key role of RST is to transform the features with the help of three particular 1x1Convolutions while enhancing the discriminability. The experiment was conducted with three datasets (considering only thermal probe): the polarimetric thermal [42], the polarimetrics thermal extended to 111 subjects [11], [42]-*ext.* and a private dataset containing paired visible/thermal faces of 126 subjects. DAF is mainly compared to DPM [89] and show significant improvement.

Axial-GAN. Immidisetti *et al.* [107] proposed Axial-Generative Adversarial Network (Axial-GAN) to synthesize high-resolution visible images from low-resolution thermal counterparts. The proposed GAN framework designed an axial-attention layer with transformer to model long-range dependencies to facilitate long-distance face matching. Their work can simultaneously address face hallucination and translation for thermal-to-visible face matching. Evaluations on ARL-VTF thermal and multi-modal polarimetric thermal face recognition datasets obtained promising performances compared to SAGAN and HiFaceGAN.

LG-GAN. Anghelone *et al.* [108] proposed a Latent-Guided Generative Adversarial Network (LG-GAN) which disentangle the identity from other confounding factors. Hence, an input face image is explicitly decomposed into an *identity latent code* that is spectral-invariant and a *style latent code* that is spectral-dependent. Thermal-to-Visible translation is performed by switching the thermal style code with the opposite visible style code and recombined

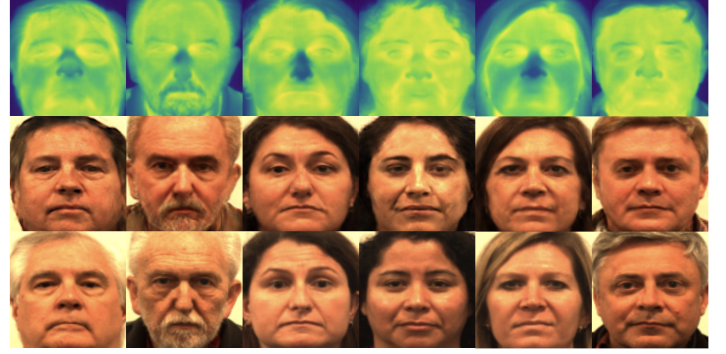


Fig. 16: **Synthesizing VIS face images** from thermal images on ARL-VTF dataset [99] using LG-GAN method. Top row is the thermal input, middle row is the LG-GAN generation and bottom row is the ground truth image.

with the identity code. Interpretation of the identity code offers useful insights in explaining salient facial structures that are essential to generate high-fidelity face images. By using such disentanglement, LG-GAN is able to preserve the identity during the spectral transformation and thus achieve promising face recognition results with respect to visual quality (Figure 16).

ATC. Peri *et al.* [94] presented a comprehensive study on synthesis-based approach for thermal-to-visible face verification. They explored Pix2Pix, CycleGAN and Contrastive Unpaired Translation (CUT) off-the-shelf domain adaptation algorithms for the task of generating realistic synthetic samples. They further demonstrated that additional custom loss such as Pixel wise correspondence loss and identity loss are instrumental for addressing the thermal-to-visible face verification. Authors highlighted the impact of the face alignment and encompass their method named ATC with above loss functions in a end-to-end thermal-to-visible system comprising ATC: Alignment, spectrum Translation and Classification steps.

Summary of LWIR-to-VIS Face Comparison

LWIR-to-VIS CFR scenario resembles MWIR-to-VIS CFR scenario as face images captured in LWIR and MWIR spectral bands are almost indistinguishable. In the previous works of MWIR-to-VIS comparison, algorithms developed based on Pix2Pix have been used to address the challenge [10], [59]. The Pix2Pix model was designed only to learn forward mapping from one domain to another, while CycleGAN was streamlined to learn both the forward and inverse mappings simultaneously using cycle-consistency loss. In the work of [70], CycleGAN was used to learn such bi-directional mappings for LWIR and VIS face images. The objective function of CycleGAN is defined as

$$\begin{aligned} \mathcal{L}(G, F, D_X, D_Y) = & \mathcal{L}_{GAN}(G, D_Y, X, Y) \\ & + \mathcal{L}_{GAN}(F, D_X, Y, X) \\ & + \lambda \mathcal{L}_{cyc}(G, F). \end{aligned} \quad (20)$$

Here, G is used to learn the forward mapping from X to Y , i.e., $G : \{X \rightarrow Y\}$. The corresponding discriminator is D_Y .

Therefore, $\mathcal{L}_{GAN}(G, D_Y, X, Y)$ can be described by

$$\begin{aligned} \mathcal{L}_{GAN}(G, D_Y, X, Y) &= \mathbb{E}_{y \sim p_{data}(y)} [\log(D_Y(y))] \\ &+ \mathbb{E}_{x \sim p_{data}(x)} [\log(1 - D_Y(G(x)))]. \end{aligned} \quad (21)$$

Similarly, F is used to learn the inverse mapping from Y to X , i.e., $F : \{Y \rightarrow X\}$. The corresponding discriminator is D_X . $\mathcal{L}_{GAN}(F, D_X, Y, X)$ can be described by

$$\begin{aligned} \mathcal{L}_{GAN}(F, D_X, Y, X) &= \mathbb{E}_{x \sim p_{data}(x)} [\log(D_X(x))] \\ &+ \mathbb{E}_{y \sim p_{data}(y)} [\log(1 - D_X(G(y)))]. \end{aligned} \quad (22)$$

In addition to adversarial losses of $\mathcal{L}_{GAN}(G, D_Y, X, Y)$ and $\mathcal{L}_{GAN}(F, D_X, Y, X)$, a cycle consistency loss was also introduced to ensure that an input image x in domain X can be successfully reconstructed after going through both the forward mapping G and the inverse mapping F , i.e., $x \rightarrow G(x) \rightarrow F(G(x)) \rightarrow \bar{x}$. The cycle consistency loss is described by

$$\begin{aligned} \mathcal{L}_{cyc}(G, F) &= \mathbb{E}_{x \sim p_{data}(x)} \|F(G(x)) - x\|_1 \\ &+ \mathbb{E}_{y \sim p_{data}(y)} \|G(F(y)) - y\|_1. \end{aligned} \quad (23)$$

Using CycleGAN alone allowed the generation of visually pleasant visible images from thermal images. However, adding more constraints to restrict the mappings is envisioned further improve the synthesis quality. In [70], a 68-point landmark detection network was used to extract the landmarks from the visible images. This can assist the CycleGAN to preserve the geometrical shapes of the reconstructed samples. The shape loss was defined as

$$\mathcal{L}_{shape} = \frac{1}{68} [(y_s - G(x)_s)^2 + (y_s - F(G(y))_s)^2], \quad (24)$$

where, x is a thermal image and $G(x)$ is a synthesized visible image from generator G . y is a visible image and $F(G(y))$ is a reconstructed visible image.

7.3 Longwave with polarimetry

Polarimetric imagery in the thermal band has shown several advantages, particularly in bringing more details for both geometrical and textural information. In addition, **Experiment 2** with Table 1 were designed to show the effectiveness of algorithms in comparing face. All LWIR polarimetry-to-VIS face comparison performance are reported on the Table 7 and timeline of developments in algorithms are summarized in the Figure 17.

GAN-VFS. Zhang *et al.* [98] proposed a *Generative Adversarial Network-based Visible face Synthesis* (GAN-VFS) algorithm to synthesize visible face images from their corresponding polarimetric images. The proposed GAN-VFS method contained three different modules, including visible feature extraction module, guidance sub-network module and visible image reconstruction module. The visible feature extraction module was used to extract the visible features from the raw polarimetric image. The guidance sub-network module ensured that extracted visible features were instrumental in reconstructing visible images. The output of the guidance subnetwork constituted the guided features, which were finally used to reconstruct the visible image.

This was optimized by the combination of identity loss and perceptual loss.

AP-GAN. Di *et al.* [61] proposed an *Attribute Preserved Generative Adversarial Network* (AP-GAN) to synthesize the visible image from the polarimetric thermal image. A pre-trained VGG-Face model was first used to extract the attributes from the visible face image. Then, the extracted attributes were used as a prior to ensure that the synthesized visible face image from the polarimetric thermal image would share similar attributes. Finally, a pre-trained FR network was used to extract features from both visible and synthesized visible face images for comparison.

CpDCNN. Iranmanesh *et al.* [101] presented a *Coupled Deep Convolutional Neural Network* (CpDCNN) to find and hence learn deep global discriminative features between polarimetric LWIR image faces and the corresponding visible faces. They used both thermal and polarimetric state information to bring more detail and then enhance the performance of thermal-to-visible CFR scenario. Their method was based on two VGG-16 coupled architectures, one *Vis-DCNN* pretrained on the Imagenet dataset, dedicated to the visible spectrum and another one *Pol-DCNN* initialized with the former one weights, focused to the polarimetric LWIR imagery. Together, Vis-DCNN and Pol-DCNN were linked via a *contrastive* loss function \mathcal{L}_{ct} .

MS-GAN. Zhang *et al.* [11] were interested to synthesize high-quality visible images from polarimetric thermal images in order to generate photo realistic visible face images. Note that authors previous work **GAN-VFS** [98] had addressed the same problem. Therefore, they presented a new *Multi-Stream feature-level* (MS-GAN) fusion method based on GAN. The proposed architecture consisted of a *generator* sub-network constructed using an encoder-decoder network based on dense-residual blocks, and a *discriminator* sub-network to capture features at multiple scales. Further, to ensure that the encoded features contain geometric and texture information, a deep-guided sub-network was stacked at the end of the encoding part. Figure 18a illustrates the overview of the proposed architecture and Figure 18b shows corresponding visual results. Moreover, an extended sub-dataset from [42] was collected consisting of visible and polarimetric facial signature from 111 subjects. To be consistent with previous methods [98], [109], two different protocols were introduced. Once the visible images were synthesized via the protocol presented below, the goal was to extract features in order to compare the *synthesized visible* face with a *visible* face. For the feature extraction task, they used the second last fully connected layer of the VGG-face network [110]. Best performances have been achieved with protocol 2.

SAGAN. Di *et al.* [105] proposed a synthesis network to convert between polarimetric thermal and visible images based on the *Self-Attention GAN* (SAGAN). The self-attention module was added before the last convolutional layer of the generator and it was used as a weight matrix to refine the feature maps.

DSU. Pereira *et al.* [16] suggested that high-level CNN features trained in visible spectral images was domain independent and could be used to encode faces captured in different domains. The low-level CNN features that directly connected to the input signal were domain dependent.

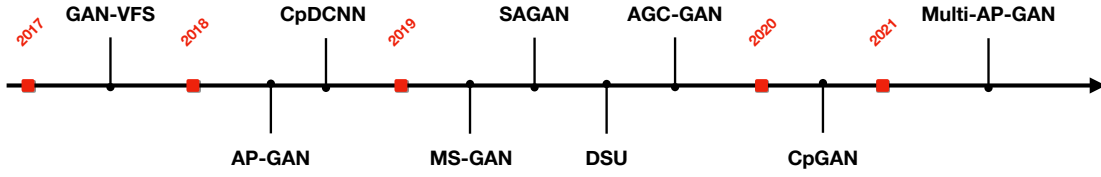


Fig. 17: **Timeline of developments in algorithms: LWIR Polarimetric-to-VIS face recognition.**

TABLE 7: Rank-1 Accuracy and Verification Rate on different dataset for the **LWIR Polarimetry-VIS** face comparison.

Year	Authors	Methods	Dataset	Performance %
2017	Zhang <i>et al.</i> [98]	GAN-VFS	Polarimetric thermal [42] - <i>Polar. Probe</i>	93.82 @Rank-1 - 79.90 @AUC - 25.17 @EER
2018	Di <i>et al.</i> [61]	AP-GAN	Polarimetric thermal [42] - <i>Polar. Probe</i>	88.93 @AUC - 19.02 @EER
	Iranmanesh <i>et al.</i> [101]	CpDCNN	Polarimetric thermal [42] - <i>Polar. Probe</i>	94.08 @Rank-1
2019	Di <i>et al.</i> [105]	SAGAN	Polarimetric thermal [42] - <i>Polar. Probe</i>	96.41 @AUC - 10.02 @EER
	Iranmanesh <i>et al.</i> [104]	AGC-GAN	Polarimetric thermal [42] - <i>Polar. Probe</i>	96.54 @Rank-1
	Zhang <i>et al.</i> [11]	MS-GAN	Polarimetric thermal [42]- <i>ext. - Polar. Probe</i>	98.00 @AUC - 7.99 @EER
2020	Iranmanesh <i>et al.</i> [66]	CpGAN	Polarimetric thermal [42] - <i>Polar. Probe</i>	95.49 @Rank-1
2021	Di <i>et al.</i> [13]	Multi-AP-GAN	Polarimetric thermal [42] - <i>Polar. Probe</i>	93.72 @AUC - 14.75 @EER

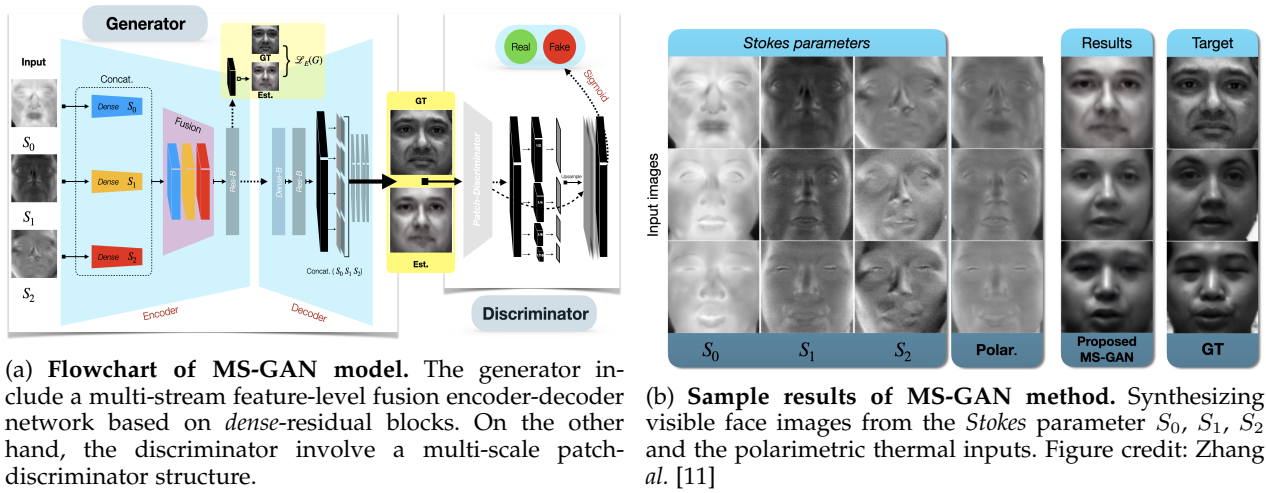


Fig. 18: **Overview of the MS-GAN [11] model: Synthesize high-quality visible images.**

These low-level features could be learned by domain specific feature detectors, termed Domain Specific Units (DSU).

AGC-GAN. Iranmanesh and Nasrabadi [104] proposed a novel *Attribute-Guided Coupled Generative Adversarial Network* (AGC-GAN) architecture that used facial attributes to improve the thermal-to-visible face recognition performance. The proposed AGC-GAN had two different generators, including Vis-GAN and Pol-GAN. The Vis-GAN and Pol-GAN were used as the generators to synthesize the corresponding visible image from the visible and polarimetric images, respectively. These two sub-networks were coupled by the contrastive loss function, aiming to find the latent feature vector that was shared by polarimetric face images and their corresponding visible ones.

CpGAN. Iranmanesh *et al.* [66] proposed a *Coupled Generative Adversarial Network* (CpGAN) depicted in Figure 19, to synthesize visible image from non-visible image such as polarimetric thermal (channel input of S_0, S_1 and S_2) for CFR task. CpGAN contained two GAN-based sub-networks, with each two appropriate generators and discriminators, dedicated to visible (Vis) and non-visible (NVis) input images. The proposed network was capable of transforming the visible and non-visible modalities into

a common discriminative embedding subspace and subsequently synthesizing the visible images from that subspace. In order to efficiently synthesize a realistic visible image from the non-visible modality, a densely connected encoder-decoder structure was used as the generator in each sub-network. The final objective of their proposed CpGAN was to learn a joint deep embedding that captured the interrelationship between the visible and non-visible facial imagery for spectrally invariant face recognition.

Multi-AP-GAN. Di *et al.* [13] proposed a novel *Multi-Scale Attribute Preserved Generative Adversarial Network* (Multi-AP-GAN) to synthesize the visible image from the polarimetric thermal image with preserved attributes. This work was an extension to their previous work on AP-GAN [61]. The attributes were extracted from visible face images by a pre-trained VGG-Face model. The Multi-AP-GAN consisted of two major components: a multimodal compact bilinear (MCB) pooling-based generator and a generator with the multi-scale architecture. The MCB pooling method was used to concatenate image feature vector and semantic attribute vector, rather than using a simple concatenation. The multi-scale generator was designed to generate multiple intermediate outputs at different resolution

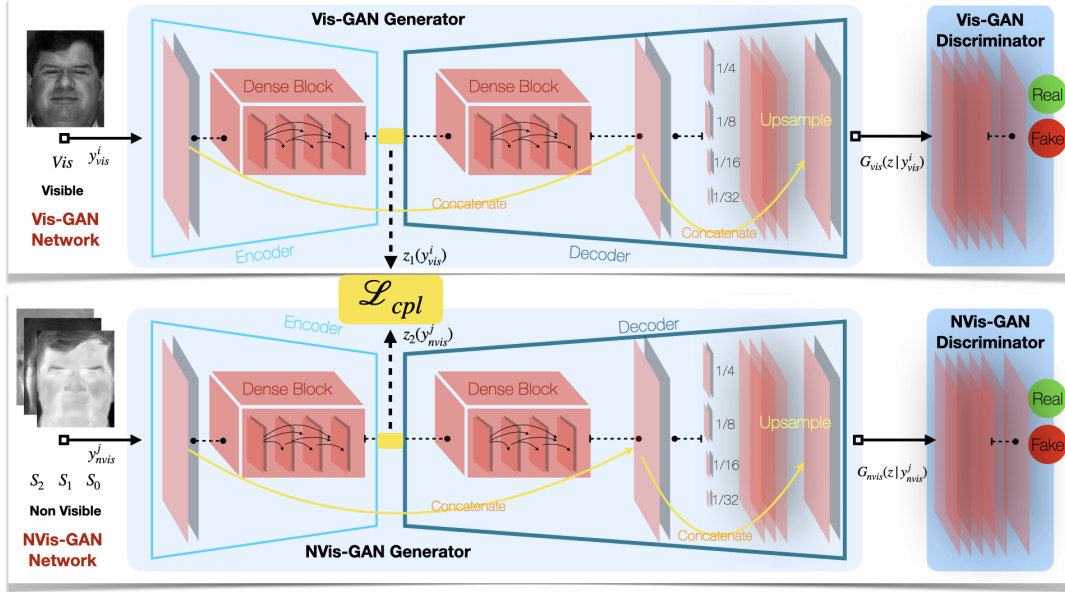


Fig. 19: Flowchart of CpGAN [66] using two GAN based sub-networks (Vis-GAN and NVis-GAN) coupled by contrastive loss function \mathcal{L}_{cpl} .

scales. The discriminator was applied to individual multi-scale resolution outputs. The proposed Multi-AP-GAN was regularized by a multi-scale adversarial loss, a perceptual loss, an identity loss and a reconstruction loss.

Summary of Polar-LWIR to VIS Face Comparison

Comparing polarimetric thermal to visible face images remains a challenge problem due to large domain discrepancy. Nearly all works have proposed GANs to synthesize visible images from the polarimetric thermal images [11], [13], [66], [105], rather than using CNNs to learn a domain-invariant feature representation. Associated GANs were based on conditional GANs, where mapping was learned from an observed image x and a random noise vector z to an output y : $G : \{x, z\} \leftrightarrow y$. The objective function of a conditional GAN is defined [95] as

$$\mathcal{L}_{GAN}(G, D) = \mathbb{E}_{x, y \sim p_{data}(x, y)}[\log D(x, y)] + \mathbb{E}_{x \sim p_{data}(x)}[\log(1 - D(x, G(x)))], \quad (25)$$

where G is the generator, D is the discriminator, x is the thermal image and y is the target visible image. $p_{data}(x)$ indicates that x is from the true data distribution and $p_{data}(x, y)$ indicates that both (x, y) are from the true data distribution. The objective of generator G is to synthesize visually realistic visible face images from thermal face images, while the discriminator D is structured to distinguish the target visible face images from the synthesized ones, conditioned on the input thermal image. In other words, the input to a discriminator D is a pair of samples (x, y) . The adversarial loss function $\mathcal{L}_{GAN}(G, D)$ only ensures that we can generate synthesized visible images $G(x)$ that are "real", but it does not provide information whether the generated sample is close to the target visible image at the per-pixel level. This can be remedied by using a per-pixel loss function, L_1

$$\mathcal{L}_1 = \mathbb{E}_{x, y \sim p_{data}(x, y)} \|G(x) - y\|_1. \quad (26)$$

The final objective function is described by

$$G^* = \arg \min_G \max_D \lambda_G \mathcal{L}_{GAN}(G, D) + \lambda_1 \mathcal{L}_1(G). \quad (27)$$

Using jointly, adversarial loss $\mathcal{L}_{GAN}(G, D)$ and $\mathcal{L}_1(G)$ serves as a foundation for these proposed methods [11], [13], [66], [105]. To further improve the comparison performance, more loss functions are employed to constrain the mapping space.

8 DATASETS

Most significant research achievements made over the past decade have heavily relied on new datasets and on designing benchmarks for evaluating CFR-algorithms. As deep learning approaches are known to be data-hungry, training data and hence publicly available datasets are a pertinent key stone in the advancement of CFR. We proceed to review such existing datasets, grouping them with respect to spectral bands, in which images were acquired. We summarize discussed datasets in Table 8. Figure 20 illustrates samples from representative CFR-datasets.

NIR-VIS. The *CASIA HFB* [78] is an early benchmark dataset developed for CFR. *CASIA HFB* comprises of 57 male and 43 female individuals (100 in total). Per subject 4 NIR and 4 VIS face images, as well as a 3D depth image have been acquired. *CASIA NIR-VIS 2.0* [41] is an extension to the *CASIA HFB* dataset and constitutes one of the first large NIR-VIS face dataset, containing 17,580 NIR-VIS face images of 725 subjects with variations in pose, expressions, eyeglasses, and distances. Compared to HFB, NIR-VIS 2.0 has several important features: (a) the number of subjects has a threefold increase; (b) the age distribution of the subjects is significantly larger; and (c) an evaluation protocol was proposed for benchmarking. Based on these dataset properties, *CASIA NIR-VIS 2.0* has been the most widely used benchmark dataset for evaluating NIR-VIS CFR. In addition to *CASIA HFB* and *NIR-VIS 2.0* datasets, there also exist benchmark datasets that exhibit other properties. The *Oulu-CASIA NIR-VIS* dataset [76] is composed of 80

subjects with six expression variations (anger, disgust, fear, happiness, sadness, and surprise). As the facial images of this database are captured under different environments from two institutes, the related illumination conditions differ slightly. We note that compared to *CASIA NIR-VIS 2.0*, *Oulu-CASIA NIR-VIS* is more suitable to study NIR-VIS CFR under facial expression changes. In addition, per subject 48 VIS samples and 48 NIR samples are provided. The *BUAA-VisNir* dataset [77] is often used for domain adaptation evaluation. This dataset contains 150 subjects, with 9 VIS images and 9 NIR images of each subject that correspond to 9 distinct poses or expressions. The training set and testing set are composed of 900 images of 50 subjects and 1800 images of the remaining 100 subjects, respectively. This evaluation protocol is more challenging due to the larger pose and illumination variations observed between the training and test sets. To alleviate the issues mentioned above, a new Large-Scale Multi-Pose High-Quality database *LAMP-HQ* [111] containing over 73000 images from 573 individuals with large diversities in pose, illumination, attribute, scene, and accessory was proposed. Nevertheless, these datasets have yet to address the problem of outdoor CFR at a long distance. The *LDHF-DB* dataset [112] offers subjects captured at distances of 60 meters, 100 meters, and 150 meters, in both VIS and NIR spectral bands. Therefore, *LDHF-DB* is highly instrumental in investigating cross-distance and cross-spectral NIR-VIS FR.

SWIR-VIS. The *PRE-TINDERS* [113] dataset is composed of 48 frontal face subjects and a total of 384 images captured at two wavelengths: visible spectrum and SWIR spectrum at 1550 nm. 4 images per subject are available for each spectral band: 2 images have neutral expression and 2 images depict the person talking (open mouth). All images in this dataset are acquired at close distance from the camera (about 2 meters) in a single session. A light source at 1550 nm is illuminating the face of the subjects for images captured in the SWIR spectral band. The original resolutions of the acquired images before normalization are 640×512 for SWIR images and 1600×1200 for visible images. The *TINDERS* [113] dataset is composed of 48 frontal face subjects having images at the same two spectral bands. The SWIR images are acquired at two long ranges (50 and 106 meters). At both distances, 4 or 5 images per class are available: two/three entail neutral expression and two have talking expression. A total of 478 images are available in the SWIR band. The visible (color) images were collected at a short distance and in two sessions (3 images per session), and all of them have neutral expression, resulting in a total of 288 images. The original resolutions of images before normalization are 640×512 for SWIR images and 640×480 for visible images.

MWIR-VIS. The *WSRI* dataset [93] comprises of 1615 visible and 1615 MWIR images from 64 subjects. There are 25 images per individual including different facial expressions. Visible images were captured at resolution 1004×1004 , while MWIR images were captured at resolution 640×512 . Face images from both modalities were preprocessed, being resized to 235×295 pixels. Training and testing set were split randomly into a set of 10 subjects and 54 subjects, respectively. *MILAB-VTF(B)* [94] is the largest collection of long-range unconstrained paired MWIR-Visible

face images, including 400 different identities with both, indoor and outdoor acquisitions.

LWIR-VIS. The *UND X1* dataset [96] contains LWIR and visible images related to 241 subjects with different variations in lighting, expression and time lapse. The original resolutions of the images are 1600×1200 pixels for the visible modality and 320×240 pixels for the LWIR modality. Both modalities are resampled to 150×110 pixels after preprocessing. The training set composed of 159 subjects was captured in the visible and LWIR modalities, with only one image per subject. On the other hand, the test set contained remaining 82 subjects with multiple images per subject. This database is challenging due to the low resolution and noise present in the LWIR imagery. This leads to significant difference between the two modalities in this dataset. The *TUFTS* [9] dataset contains over 10,000 images from 113 individuals. Images were acquired in various modalities, including visible, thermal images, near infrared images images of individual face. The *EURECOM* [102] dataset contains seven different facial variations, five different illumination conditions, five different types of occlusions, and four different head poses that belong to 50 subjects. In total, there are 2100 images in the dataset. The *ARL-VTF* [99] dataset is the newest and largest collection of time-synchronized visible-thermal face images presented in this survey. The dataset includes 395 subjects and 549,712 images with variations in expression, pose and eyewear. *ARL-VTF* is endowed with annotations, metadata as well as standardized protocols for fair evaluation.

Polar-VIS. The *Polarimetric Thermal Face* dataset [42] (also called *ARL-MMFD*) contains polarimetric LWIR and visible face images of 60 subjects, later extended to 111 subjects [11]. Data was collected at three different distances: Range 1 (2.5 m), Range 2 (5 m), and Range 3 (7.5 m). At each range, baseline and expressions data were collected and annotated. In the baseline condition, the subject was asked to maintain a neutral expression while looking at the polarimetric thermal sensor. On the other hand, in the expression condition, the subject was asked to count numerically upwards from one, resulting in different expressions in the mouth to eye regions. Each subject has 16 images of visible and 16 polarimetric LWIR images in which four images are from the base-line condition and the remaining 12 images are from the expression condition.

Multiple-Spectral. The *NVESD* dataset [90] was collected jointly by the U.S. Army *NVESD* in 2013 from 50 different subjects in different scenarios and settings including physical exercise (fast walk) and different ranges (1m, 2m and 4m). The dataset is composed of 450 images in each modality. The images were captured simultaneously from different identities with the original resolution of 640×480 pixels for all of the modalities. After preprocessing, the image resolution is resampled to 174×174 and the dataset is split into training and testing sets.

In-the-Wild Dataset. The *Thermal Faces in the Wild* (TFW) dataset [114] was the first dataset collected in both indoor and outdoor environments under controlled and in-the-wild conditions, respectively. The TFW dataset includes 145 subjects and a total of 9202 images with variation in pose. In addition, images are associated with manually labeled bounding boxes and five facial landmarks.

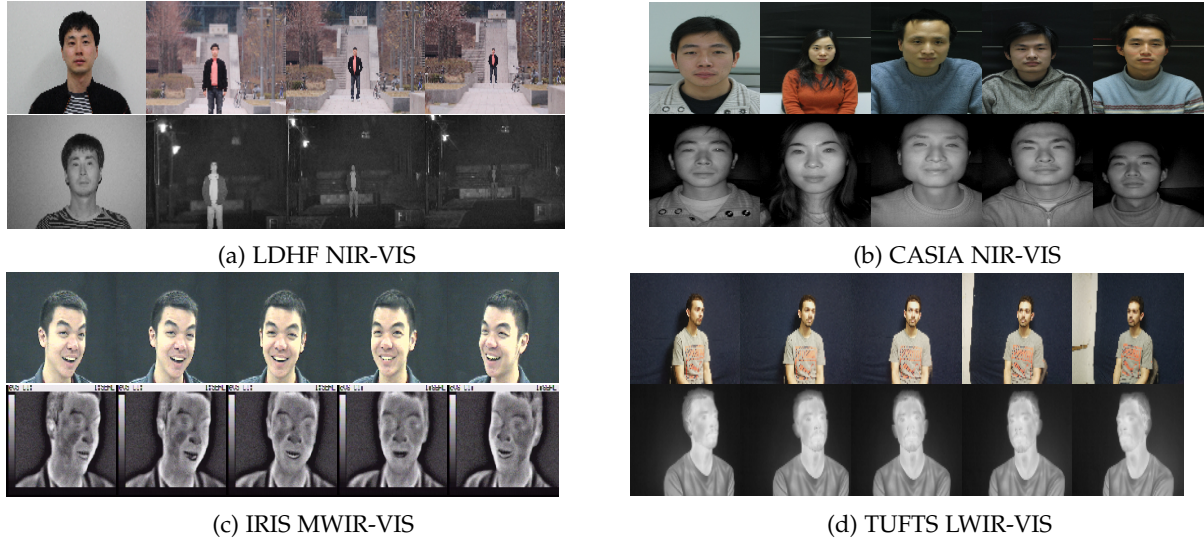


Fig. 20: Illustration of heterogeneous face recognition datasets.

TABLE 8: A quick reference summary of the main databases of face images acquired in the infrared spectrum.

Year	Name	Ref.	Spectrum						Number of		
			Vis	NIR	SWIR	MWIR	LWIR	Pola.	Subjects	Images	
2003	UND X1	[96]	✓					✓		82	4584
2006	IRIS-M3	[115]	✓					✓		82	2624
2009	Oulu-CASIA NIR-VIS	[76]	✓	✓						80	7680
	CASIA HFB	[78]	✓	✓						200	5097
2010	TINDERS	[113]	✓		✓					48	1255
	USTC-NVIE	[116]	✓					✓		103	7460
	PolyU-NIR	[117]		✓						335	34000
2011	PRE-TINDERS	[113]	✓		✓					48	576
2012	BUAA-VisNir	[77]	✓	✓						150	2700
	LDHF-DB	[112]	✓	✓						100	-
	Equinox	[118]	✓		✓	✓	✓			90	25000
	IRIS	[91]	✓				✓			32	8456
2013	NVESD	[90]	✓		✓	✓	✓			50	900
	CASIA NIR-VIS 2.0	[41]	✓	✓						725	17580
	Carl Database	[97]	✓	✓				✓		41	7380
	PCSO	[92]	✓					✓		1003	3011
2015	ND-NIVL	[119]	✓	✓						574	24605
2016	Polarimetric thermal	[42]	✓					✓	✓	60	14400
2018	EURECOM	[102]	✓					✓		50	2100
	UL-FMTV	[120]	✓			✓				238	-
2020	LAMP-HQ	[111]	✓	✓						573	73616
	Tufts	[9]	✓	✓				✓		113	10000
	HQ-WMCA	[22]	✓	✓	✓			✓		51	58080
2021	ARL-VTF	[99]	✓					✓		395	549712
	MILAB-VTF(B)	[94]	✓			✓				400	-
	TFW	[114]						✓		145	9202
-	WSRI	[93]	✓			✓				64	3230

9 OPEN RESEARCH CHALLENGES

Despite significant achievements, CFR still faces a number of challenges. In this section, we proceed to identify and discuss some pertinent challenges that are essential for further success of CFR.

Scarcity of datasets. Unlike traditional FR, where millions of faces can be leveraged to train deep learning based models, CFR remains significantly impeded by lack of large-scale heterogeneous face datasets. In addition, very few existing datasets are endowed with annotations of face bounding box and landmarks [38]. Such annotations are essential

in developing automated face and landmark detection for CFR.

Large standoff distance. Limited work has focused on CFR at large standoff distances [112]. Most existing works have focused on CFR, with the assumption that faces have been captured at a short standoff distance. However, capturing faces at large standoff distances results in face image quality degradation, including low-resolution, blur and noise. Early attempts towards addressing this challenge have sought to restore high-quality images from degraded ones [112], [121]. Such methods were developed by learning a locally linear mapping between low-quality patches and

high-quality patches. The linear mapping assumption has been relaxed on patch-level, while in practice, mapping is often considered to be non-linear. In this context, it has been demonstrated that GANs have been highly suitable to model non-linear mappings.

Modality gap. The key problem with CFR is the apparent disparity between visible and invisible spectrum, and this strongly impacts the comparison performance (see Experiment 2). Although cross-spectrum featured-based methods, such as *transfer learning* or *domain adaptation* have achieved good results, especially in the *Active IR* band, such methods remain less efficient in the *Passive IR* band. An obvious solution is to incorporate details with regard to both geometrical and textural information. Unsupervised-processing methods with deep generative models, such as cross-spectrum images synthesis, appear to be the trend, in particular as a result of GAN-improvement. So far, "synthetic data" has not yet outperformed the CFR state-of-the-art, but we foresee promising results.

Privacy. Infrared imaging is a keystone biometric solution in terms of security and privacy [6]. Firstly, humans are not able to recognize someone as the IR-appearance does not resemble RGB-images (Figure 4). Secondly, it allows to ensure pseudo-anonymized recognition and compliance with legal requirements regarding personal data, as well as template protection. Finally, IR is robust to attempted diversion and spoofing attacks, as artifacts are directly identifiable by appearing differently on face images. While intuitive, the above has not been studied rigorously in scientific literature.

Presentation Attacks. FR systems have shown to be vulnerable to presentation attacks, where an adversarial uses artifacts such as print, video replay, makeup and 3D mask to undermine the system. Reflection difference between live faces and spoof faces under NIR [122], [123], SWIR [124] or LWIR [8] spectral bands can be exploited to detect such presentation attacks. CFR can provide a unique insight, complementing RGB-imagery, as it imparts liveness detection, as well as shape determination [22].

10 SUMMARY

In this article, we reviewed methods that have been developed in CFR, placing emphasis on recent deep CNN-architectures. We discussed associated benefits and limitations, as well as employed datasets. CFR is endowed with the ability to identify people in challenging illumination settings, as well as to detect presentation attacks. Such benefits have been exploited in applications including *defense*, *surveillance* and *public safety*.

While traditional FR is restricted to compare images in the visible spectrum, CFR is inherently more challenging, as both identification, as well as spectral variation have to be addressed. In order to separate spectral variation from identity, approaches such as domain-invariant feature representation have been proposed. Despite such CNN-based approaches usually performing well in minimizing spectral variation between NIR and visible spectral bands, a large modality gap introduced by capturing face images in the thermal spectral band can be overcome employing GANs.

In CNN-based approaches, streamlined to learn domain-invariant features, *triplet* loss function has demonstrated better performance than the *contrastive* loss function, since

the former considers both, intra-class minimization and inter-class maximization. For GAN-based approaches, the *identity* loss function is essential to ensure that synthesized faces preserve the same identity as the ground-truth face. Other loss functions such as *attribution loss*, *shape loss* or *semantic loss* are considered as auxiliary loss functions.

In case of spectral band selections, NIR is preferred for reflective IR-to-Visible FR in the majority of applications. There is not much difference between MWIR or LWIR spectral bands in emissive IR-to-Visible FR. Nevertheless, the use of polarimetry for LWIR has been attributed higher face comparison results. While NIR and SWIR spectral bands can produce relatively good face resolutions, this remains a challenge for MWIR and LWIR sensors. Towards improving poor resolution associated with thermal images, there is a necessity to develop high-resolution sensors by integrating super-resolution post-processing schemes. CFR has been impeded by lack of publicly available face datasets. With the emergence of more comprehensive and large-scale datasets, such as ARL-VTF [99] and MILAB-VTF(B) [94], we foresee the performance of CFR further improving.

To conclude, CFR has several challenging issues, and this survey has shown that the research community has an indiscriminate need for systematic research in that field, rather than empirical experimentation with different loss functions and networks. Such concerns necessitate the introduction of robust and reliable methods to identify forged images and videos.

REFERENCES

- [1] W. Zhao, R. Chellappa, P. J. Phillips, and A. Rosenfeld. Face recognition: A literature survey. *ACM Computing Surveys*, 35(4):399–458, 2003.
- [2] A. F. Abate, M. Nappi, D. Riccio, and G. Sabatino. 2D and 3D face recognition: A survey. *Pattern Recognition Letters*, 28(14):1885 – 1906, 2007.
- [3] S. Z. Li and A. K. Jain, editors. *Handbook of Face Recognition*. Springer London, 2011.
- [4] Mei Wang and Weihong Deng. Deep face recognition: A survey. *Neurocomputing*, 2020.
- [5] Y. Taigman, M. Yang, M.A. Ranzato, and L. Wolf. Deepface: Closing the gap to human-level performance in face verification. In *IEEE Conference on Computer Vision and Pattern Recognition*, pages 1701–1708, 2014.
- [6] S. Hu, N. Short, B.S. Riggan, M. Chasse, and M.S. Sarfraz. Heterogeneous face recognition: recent advances in infrared-to-visible matching. In *IEEE International Conference on Automatic Face & Gesture Recognition*, pages 883–890, 2017.
- [7] T. Bourlai and L.A. Hornak. Face recognition outside the visible spectrum. *Image and Vision Computing*, 55:14 – 17, 2016.
- [8] L. Spinoulas, M. E. Hussein, D. Geissbühler, J. Mathai, O. G. Almeida, G. Clivaz, S. Marcel, and W. Abdalmageed. Multispectral biometrics system framework: Application to presentation attack detection. *IEEE Sensors Journal*, 21(13):15022–15041, 2021.
- [9] K. Panetta, Q.W. Wan, S. Agaian, S. Rajeev, S. Kamath, R. Rajendran, S.P. Rao, A. Kaszowska, H.A. Taylor, A. Samani, and X. Yuan. A comprehensive database for benchmarking imaging systems. 42(3):509–520, 2020.
- [10] C. Chen and A. Ross. Matching thermal to visible face images using a semantic-guided generative adversarial network. In *IEEE International Conference on Automatic Face & Gesture Recognition*, pages 1–8, 2019.
- [11] H. Zhang, B.S. Riggan, S. Hu, N. J. Short, and V. M. Patel. Synthesis of high-quality visible faces from polarimetric thermal faces using generative adversarial networks. *International Journal of Computer Vision*, 127(6-7):845–862, 2019.
- [12] R. He, J. Cao, L. Song, Z. Sun, and T. Tan. Cross-spectral face completion for NIR-VIS heterogeneous face recognition. *ArXiv*, abs/1902.03565, 2019.

- [13] Xing Di, Benjamin S. Riggan, Shuowen Hu, Nathaniel J. Short, and Vishal M. Patel. Multi-scale thermal to visible face verification via attribute guided synthesis. *IEEE Trans. Biom. Behav. Identity Sci.*, 3(2):266–280, 2021.
- [14] R.S. Ghiass, O. Arandjelović, A. Bendada, and X. Maldague. Infrared face recognition: A comprehensive review of methodologies and databases. *Pattern Recognition*, 47(9):2807–2824, 2014.
- [15] R. Munir and R.A. Khan. An extensive review on spectral imaging in biometric systems: Challenges & advancements. *Journal of Visual Communication and Image Representation*, 65, 2019.
- [16] T. de Freitas Pereira, A. Anjos, and S. Marcel. Heterogeneous face recognition using domain specific units. *IEEE Transactions on Information Forensics and Security*, 14(7):1803–1816, 2019.
- [17] K. Weiss, T.M. Khoshgoftaar, and D. Wang. A survey of transfer learning. *Journal of Big data*, 3(1):9, 2016.
- [18] A.K. Jain, A. Ross, and S. Prabhakar. An introduction to biometric recognition. *IEEE Transactions on circuits and systems for video technology*, 14(1):4–20, 2004.
- [19] A. Prati, C. Shan, and K. I-K Wang. Sensors, vision and networks: From video surveillance to activity recognition and health monitoring. *Journal of Ambient Intelligence and Smart Environments*, 11(1):5–22, 2019.
- [20] M. Krišto and M. Ivacic-Kos. An overview of thermal face recognition methods. In *International Convention on Information and Communication Technology, Electronics and Microelectronics*, pages 1098–1103, 2018.
- [21] A. George and S. Marcel. Can your face detector do anti-spoofing? face presentation attack detection with a multi-channel face detector, 2020.
- [22] G. Heusch, A. George, D. Geissbühler, Z. Mostaani, and S. Marcel. Deep models and shortwave infrared information to detect face presentation attacks. *IEEE Transactions on Biometrics, Behavior, and Identity Science*, 2020.
- [23] S. Ouyang, T. Hospedales, Y.Z. Song, X. Li, C.C. Loy, and X. Wang. A survey on heterogeneous face recognition: Sketch, infra-red, 3D and low-resolution. *Image and Vision Computing*, 56:28–48, 2016.
- [24] L.B. Wolff, D.A. Socolinsky, and C.K. Eveland. Face recognition in the thermal infrared. In *Computer Vision Beyond the Visible Spectrum*, pages 167–191. 2005.
- [25] P. Buddharaju, I. T. Pavlidis, P. Tsiamyrtzis, and M. Bazakos. Physiology-based face recognition in the thermal infrared spectrum. *IEEE Transactions on Pattern Analysis and Machine Intelligence*, 29(4):613–626, 2007.
- [26] S.G. Kong, J. Heo, B.R. Abidi, J. Paik, and M.A. Abidi. Recent advances in visual and infrared face recognition review. *Computer Vision and Image Understanding*, 97(1):103–135, 2005.
- [27] M.K. Bhowmik, K. Saha, S. Majumder, G. Majumder, A. Saha, A.N. Sarma, D. Bhattacharjee, D. K. Basu, and M. Nasipuri. Thermal infrared face recognition—a biometric identification technique for robust security system. *Reviews, refinements and new ideas in face recognition*, 7, 2011.
- [28] N. Narang, T. Bourlai, and L.A. Hornak. Can we match ultraviolet face images against their visible counterparts? In *Algorithms and Technologies for Multispectral, Hyperspectral, and Ultraspectral Imagery XXI*, volume 9472, page 94721Q. International Society for Optics and Photonics, 2015.
- [29] Z. Wang, A. C. Bovik, H. R. Sheikh, and E. P. Simoncelli. Image quality assessment: from error visibility to structural similarity. *IEEE Transactions on Image Processing*, 13(4):600–612, 2004.
- [30] S. Z. Li, R. Chu, S. Liao, and L. Zhang. Illumination invariant face recognition using near-infrared images. *IEEE Transactions on Pattern Analysis and Machine Intelligence*, 29(4):627–639, 2007.
- [31] F. Nicolo and N. A. Schmid. Long range cross-spectral face recognition: Matching SWIR against visible light images. *IEEE Transactions on Information Forensics and Security*, 7(6):1717–1726, 2012.
- [32] S. Heist, M. Landmann, M. Steglich, Y. Zhang, P. KÄEhmstedt, and G. Notni. Pattern projection in the short-wave infrared (SWIR): accurate, eye-safe 3D shape measurement. In *Dimensional Optical Metrology and Inspection for Practical Applications VIII*, volume 10991, pages 99–108, 2019.
- [33] T. Bourlai. Mid-wave IR face recognition systems. *SPIE Newsroom Magazine-Defense & Security*, 2013.
- [34] J L. Pezzaniti and D.B. Chenault. Polarization imaging for facial recognition enhancement system and method, 2020. US Patent App. 16/431,374.
- [35] W. Liu, Y. Wen, Z. Yu, M. Li, B. Raj, and L. Song. Sphreface: Deep hypersphere embedding for face recognition, 2017.
- [36] J. Deng, J. Guo, N. Xue, and S. Zafeiriou. Arcface: Additive angular margin loss for deep face recognition. In *IEEE Conference on Computer Vision and Pattern Recognition*, pages 4690–4699, 2019.
- [37] D. Poster, S. Hu, N. Nasrabadi, and B. Riggan. An examination of deep-learning based landmark detection methods on thermal face imagery. In *IEEE Conference on Computer Vision and Pattern Recognition Workshops*, pages 980–987, 2019.
- [38] M. Kopaczka, R. Kolk, J. Schock, F. Burkhard, and D. Merhof. A thermal infrared face database with facial landmarks and emotion labels. *IEEE Transactions on Instrumentation and Measurement*, 68(5):1389–1401, 2019.
- [39] W. Chu and Y. Liu. Thermal facial landmark detection by deep multi-task learning. In *IEEE International Workshop on Multimedia Signal Processing*, pages 1–6, 2019.
- [40] K. Zhang, Z. Zhang, Z. Li, and Y. Qiao. Joint face detection and alignment using multitask cascaded convolutional networks. *IEEE Signal Processing Letters*, 23(10):1499–1503, 2016.
- [41] S.Z. Li, D. Yi, Z. Lei, and S. Liao. The CASIA NIR-VIS 2.0 face database. In *IEEE Conference on Computer Vision and Pattern Recognition Workshops*, 2013.
- [42] S. Hu, N.J. Short, B.S. Riggan, C. Gordon, K.P. Gurton, M. Thielke, P. Gurrin, and A.L. Chan. A polarimetric thermal database for face recognition research. In *IEEE Conference on Computer Vision and Pattern Recognition Workshops*, 2016.
- [43] Domenick D. Poster, Shuowen Hu, Nathan J. Short, Benjamin S. Riggan, and Nasser M. Nasrabadi. Visible-to-thermal transfer learning for facial landmark detection. *IEEE Access*, 9:52759–52772, 2021.
- [44] C. Reale, N.M. Nasrabadi, H. Kwon, and R. Chellappa. Seeing the forest from the trees: A holistic approach to near-infrared heterogeneous face recognition. pages 320–328, 2016.
- [45] R. He, X. Wu, Z. Sun, and T. Tan. Learning invariant deep representation for nir-vis face recognition. In *AAAI Conference on Artificial Intelligence*, page 2000–2006, 2017.
- [46] R. He, X. Wu, Z. Sun, and T. Tan. Wasserstein cnn: Learning invariant features for nir-vis face recognition. *IEEE transactions on pattern analysis and machine intelligence*, 41(7):1761–1773, 2018.
- [47] X. Liu, L. Song, X. Wu, and T. Tan. Transferring deep representation for NIR-VIS heterogeneous face recognition. pages 1–8, 2016.
- [48] Karen Simonyan and Andrew Zisserman. Very deep convolutional networks for large-scale image recognition. In *International Conference on Learning Representations*, 2015.
- [49] J. Lezama, Q. Qiu, and G. Sapiro. Not afraid of the dark: NIR-VIS face recognition via cross-spectral hallucination and low-rank embedding. In *IEEE Conference on Computer Vision and Pattern Recognition*, 2017.
- [50] M. Bihn, M. Gunther, D. Lemmond, and T. Boulton. Evaluating a convolutional neural network on short-wave infra-red images. In *IEEE Winter Applications of Computer Vision Workshops*, pages 18–27, 2018.
- [51] L. Kezebou, V. Oludare, K. Panetta, and S. Agaian. TR-GAN: thermal to RGB face synthesis with generative adversarial network for cross-modal face recognition. In *Mobile Multimedia/Image Processing, Security, and Applications*, volume 11399, pages 158–168. SPIE, 2020.
- [52] C. Szegedy, W. Liu, Y. Jia, P. Sermanet, S. Reed, D. Anguelov, D. Erhan, V. Vanhoucke, and A. Rabinovich. Going deeper with convolutions. In *IEEE conference on Computer Vision and Pattern Recognition*, pages 1–9, 2015.
- [53] Ka. He, X. Zhang, S. Ren, and J. Sun. Deep residual learning for image recognition. In *IEEE conference on Computer Vision and Pattern Recognition*, pages 770–778, 2016.
- [54] B. Cao, N. Wang, X. Gao, J. Li, and Z. Li. Multi-margin based decorrelation learning for heterogeneous face recognition. In *International Joint Conference on Artificial Intelligence*, pages 680–686, 2019.
- [55] Z. Deng, X. Peng, Z. Li, and Y. Qiao. Mutual component convolutional neural networks for heterogeneous face recognition. *IEEE Transactions on Image Processing*, 28(6):3102–3114, 2019.
- [56] M. Cho, T. Kim, I.J. Kim, and S. Lee. Relational deep feature learning for heterogeneous face recognition. *IEEE Transactions on Information Forensics and Security*, 16:376–388, 2020.
- [57] O. Ronneberger, P. Fischer, and T. Brox. U-net: Convolutional networks for biomedical image segmentation. In *International Conference on Medical Image Computing and Computer Assisted Intervention*, pages 234–241, 2015.

- [58] S. Chatterjee and W.T. Chu. Thermal face recognition based on transformation by residual U-Net and pixel shuffle upsampling. In *International Conference on Multimedia Modeling*, pages 679–689, 2020.
- [59] T. Zhang, A. Wiliem, S. Yang, and B. Lovell. TV-GAN: Generative adversarial network based thermal to visible face recognition. In *2018 International Conference on Biometrics*, pages 174–181, 2018.
- [60] A. Kantarcı and H.K. Ekenel. Thermal to visible face recognition using deep autoencoders. In *2019 International Conference of the Biometrics Special Interest Group (BIOSIG)*, pages 1–5. IEEE, 2019.
- [61] X. Di, H. Zhang, and V. M. Patel. Polarimetric thermal to visible face verification via attribute preserved synthesis. In *IEEE International Conference on Biometrics Theory, Applications and Systems*, pages 1–10, 2018.
- [62] C. Szegedy, V. Vanhoucke, S. Ioffe, J. Shlens, and Z. Wojna. Rethinking the inception architecture for computer vision. In *Conference on Computer Vision and Pattern Recognition*, pages 2818–2826, 2016.
- [63] W. Hu, H. Hu, and X. Lu. Heterogeneous face recognition based on multiple deep networks with scatter loss and diversity combination. *IEEE*, 7:75305–75317, 2019.
- [64] W. Hu and H. Hu. Adversarial disentanglement spectrum variations and cross-modality attention networks for nir-vis face recognition. *IEEE Transactions on Multimedia*, pages 1–1, 2020.
- [65] G. Huang, Z. Liu, L. Van Der Maaten, and K.Q. Weinberger. Densely connected convolutional networks. In *Proceedings of the IEEE conference on computer vision and pattern recognition*, pages 4700–4708, 2017.
- [66] S.M. Iranmanesh, B. Riggan, S. Hu, and N.M. Nasrabadi. Coupled generative adversarial network for heterogeneous face recognition. *Image and Vision Computing*, page 103861, 2019.
- [67] X. Wu, R. He, Z. Sun, and T. Tan. A light cnn for deep face representation with noisy labels. *IEEE Transactions on Information Forensics and Security*, 13(11):2884–2896, 2018.
- [68] X. Wu, L. Song, R. He, and T. Tan. Coupled deep learning for heterogeneous face recognition. 2018.
- [69] I.J. Goodfellow, J. Pouget-Abadie, M. Mirza, B. Xu, D. Warde-Farley, S. Ozair, A. Courville, and Y. Bengio. Generative adversarial networks, 2014.
- [70] Z. Wang, Z. Chen, and F. Wu. Thermal to visible facial image translation using generative adversarial networks. *IEEE Signal Processing Letters*, 25(8):1161–1165, 2018.
- [71] Y. Sun, Y. Chen, X. Wang, and X. Tang. Deep learning face representation by joint identification-verification. In *Advances in neural information processing systems*, pages 1988–1996, 2014.
- [72] Y. Wen, K. Zhang, Z. Li, and Y. Qiao. A discriminative feature learning approach for deep face recognition. In *European conference on computer vision*, pages 499–515. Springer, 2016.
- [73] J. Deng, Y. Zhou, and S. Zafeiriou. Marginal loss for deep face recognition. In *IEEE Conference on Computer Vision and Pattern Recognition Workshops*, pages 60–68, 2017.
- [74] H. Wang, Y. Wang, Z. Zhou, X. Ji, D. Gong, J. Zhou, Z. Li, and W. Liu. Cosface: Large margin cosine loss for deep face recognition. In *IEEE Conference on Computer Vision and Pattern Recognition*, 2018.
- [75] I. Masi, Y. Wu, T. Hassner, and P. Natarajan. Deep face recognition: A survey. In *2018 31st SIBGRAPI Conference on Graphics, Patterns and Images (SIBGRAPI)*, pages 471–478, 2018.
- [76] J. Chen, D. Yi, J. Yang, G. Zhao, S.Z. Li, and M. Pietikainen. Learning mappings for face synthesis from near infrared to visual light images. In *IEEE Conference on Computer Vision and Pattern Recognition*, pages 156–163, 2009.
- [77] D. Huang, J. Sun, and Y. Wang. The buaa-visnir face database instructions. *School Comput. Sci. Eng., Beihang Univ., Beijing, China, Tech. Rep. IRIP-TR-12-FR-001*, 2012.
- [78] S. Z. Li, Z. Lei, and Meng Ao. The hfb face database for heterogeneous face biometrics research. In *IEEE Conference on Computer Vision and Pattern Recognition Workshops*, pages 1–8, 2009.
- [79] W. Hu and H. Hu. Disentangled spectrum variations networks for nir-vis face recognition. *IEEE Transactions on Multimedia*, 22(5):1234–1248, 2020.
- [80] W. Hu and H. Hu. Dual adversarial disentanglement and deep representation decorrelation for nir-vis face recognition. *IEEE Transactions on Information Forensics and Security*, 2020.
- [81] D. Yi, Z. Lei, S. Liao, and S.Z. Li. Learning face representation from scratch. *ArXiv*, abs/1411.7923, 2014.
- [82] W. Hu and H. Hu. Discriminant deep feature learning based on joint supervision loss and multi-layer feature fusion for heterogeneous face recognition. *Computer Vision and Image Understanding*, 184:9–21, 2019.
- [83] Chaoyou Fu, Xiang Wu, Yibo Hu, Huaibo Huang, and Ran He. Dvg-face: Dual variational generation for heterogeneous face recognition. *IEEE Transactions on Pattern Analysis and Machine Intelligence*, 2021.
- [84] Chaoyou Fu, Xiang Wu, Yibo Hu, Huaibo Huang, and Ran He. Dual variational generation for low-shot heterogeneous face recognition. *CoRR*, abs/1903.10203, 2019.
- [85] T. Bourlai and B. Cukic. Multi-spectral face recognition: Identification of people in difficult environments. In *IEEE International Conference on Intelligence and Security Informatics*, pages 196–201, 2012.
- [86] T. Bourlai, N. Kalka, A. Ross, B. Cukic, and L. Hornak. Cross-spectral face verification in the short wave infrared (swir) band. In *International Conference on Pattern Recognition*, pages 1343–1347, 2010.
- [87] N. D. Kalka, T. Bourlai, B. Cukic, and L. Hornak. Cross-spectral face recognition in heterogeneous environments: A case study on matching visible to short-wave infrared imagery. In *International Joint Conference on Biometrics*, 2011.
- [88] Z. Cao, N.A. Schmid, and T. Bourlai. Composite multilobe descriptors for cross-spectral recognition of full and partial face. *Optical Engineering*, 55(8):1–15, 2016.
- [89] M. Sarfraz and R. Stiefelagen. Deep perceptual mapping for cross-modal face recognition. *International Journal of Computer Vision*, 01 2017.
- [90] K.A. Byrd. Preview of the newly acquired nvesd-ar1 multimodal face database. In *SPIE*, volume 8734, pages 8734–8734, 2013.
- [91] University of Tennessee. Iris thermal/visible face database. <http://www.cse.ohio-state.edu/otcbvs-bench/>, 2012.
- [92] B.F. Klare and A.K. Jain. Heterogeneous face recognition using kernel prototype similarities. *IEEE transactions on pattern analysis and machine intelligence*, 35(6):1410–1422, 2013.
- [93] WRIGHT STATE Dataset. <https://wsri.wright.edu/>.
- [94] N. Peri, J. Gleason, C. D. Castillo, T. Bourlai, V. M. Patel, and R. Chellappa. A synthesis-based approach for thermal-to-visible face verification. In *2021 16th IEEE International Conference on Automatic Face and Gesture Recognition (FG 2021)*, pages 01–08, 2021.
- [95] P. Isola, J. Zhu, T. Zhou, and A. A. Efros. Image-to-image translation with conditional adversarial networks. In *IEEE Conference on Computer Vision and Pattern Recognition*, pages 5967–5976, 2017.
- [96] University of Notre Dame. University of notre dame biometric data set collection c. <https://cvrl.nd.edu/projects/data/nd-2006-dataset>, Last accessed 2012.
- [97] V. Espinosa-Duró, M. Faundez-Zanuy, and J. Mekyska. A new face database simultaneously acquired in visible, near-infrared and thermal spectrums. *Cognitive Computation*, 5:119–135, 2013.
- [98] H. Zhang, V.M. Patel, B.S. Riggan, and S. Hu. Generative adversarial network-based synthesis of visible faces from polarimetric thermal faces. In *International Joint Conference on Biometrics*, pages 100–107. IEEE, 2017.
- [99] D. Poster, M. Thielke, R. Nguyen, S. Rajaraman, X. Di, C. N. Fondje, V.M. Patel, N.J. Short, B.S. Riggan, N.M. Nasrabadi, and S. Hu. A large-scale, time-synchronized visible and thermal face dataset. In *IEEE/CVF Winter Conference on Applications of Computer Vision (WACV)*, pages 1559–1568, 2021.
- [100] J.Y. Zhu, T.g Park, P. Isola, and A.A. Efros. Unpaired image-to-image translation using cycle-consistent adversarial networks. In *IEEE international conference on computer vision*, pages 2223–2232, 2017.
- [101] S.M. Iranmanesh, A. Dabouei, H. Kazemi, and N.M. Nasrabadi. Deep cross polarimetric thermal-to-visible face recognition. In *International Conference on Biometrics*, pages 166–173. IEEE, 2018.
- [102] K. Mallat and J. Dugelay. A benchmark database of visible and thermal paired face images across multiple variations. In *International Conference of the Biometrics Special Interest Group (BIOSIG)*, pages 1–5, 2018.
- [103] K. Mallat, N. Damer, F. Boutros, A. Kuijper, and J. Dugelay. Cross-spectrum thermal to visible face recognition based on cascaded image synthesis. In *International Conference on Biometrics*, pages 1–8, 2019.
- [104] S.M. Iranmanesh and N.M. Nasrabadi. Attribute-guided deep polarimetric thermal-to-visible face recognition, 2019.

- [105] X. Di, B.S. Riggan, S. Hu, N.J. Short, and V.M. Patel. Polarimetric thermal to visible face verification via self-attention guided synthesis. In *International Conference on Biometrics*, pages 1–8. IEEE, 2019.
- [106] C. N. Fondje, S. Hu, N. J. Short, and B.S. Riggan. Cross-domain identification for thermal-to-visible face recognition. In *International Joint Conference on Biometrics*, 2020.
- [107] Rakhil Immidiseti, Shuowen Hu, and Vishal M. Patel. Simultaneous face hallucination and translation for thermal to visible face verification using axial-gan. *CoRR*, abs/2104.06534, 2021.
- [108] David Anghelone, Cunjian Chen, Philippe Faure, Arun Ross, and Antitza Dantcheva. Explainable thermal to visible face recognition using latent-guided generative adversarial network. In *IEEE International Conference on Automatic Face & Gesture Recognition, FG 2021, Jodhpur, India, Dec 15-18, 2021*. IEEE, 2021.
- [109] B. S. Riggan, N. J. Short, S. Hu, and H. Kwon. Estimation of visible spectrum faces from polarimetric thermal faces. In *IEEE International Conference on Biometrics Theory, Applications and Systems*, 2016.
- [110] O. M. Parkhi, A. Vedaldi, and A. Zisserman. Deep face recognition. In *British Machine Vision Conference*, 2015.
- [111] A. Yu, H. Wu, H. Huang, Z. Lei, and R. He. Lamp-hq: A large-scale multi-pose high-quality database for nir-vis face recognition. *arXiv preprint arXiv:1912.07809*, 2019.
- [112] H. Maeng, S. Liao, D. Kang, S.W. Lee, and A.K. Jain. Nighttime face recognition at long distance: Cross-distance and cross-spectral matching. In *ACCV*, 2012.
- [113] WVHTC Foundation Technologies Group. Pre-tinders and tinders face database. 2011.
- [114] A. Kuzdeuov, D. Aubakirova, D. Koishigarina, and H. A. Varol. Tfw: Annotated thermal faces in the wild dataset. 2021.
- [115] H. Chang H. Harishwaran M. Yi A. Koschan B. Abidi and M. Abidi. An indoor and outdoor, multimodal, multispectral and multi-illuminant database for face recognition. In *Proc. IEEE Conference on Computer Vision and Pattern Recognition Workshops*, page 54, 2006.
- [116] S. Wang, Z. Liu, S. Lv, Y. Lv, G. Wu, P. Peng, F. Chen, and X. Wang. A natural visible and infrared facial expression database for expression recognition and emotion inference. *Transactions on Multimedia*, 12(7):682–691, 2010.
- [117] B. Zhang, L. Zhang, D. Zhang, and L. Shen. Directional binary code with application to polyu near-infrared face database. *Pattern Recognition Letters*, 31:2337–2344, 10 2010.
- [118] M. Li J. Wang, S. Lai. Equinox corpotation. equinox face database. available online: <http://www.equinoxsensors.com/products/hid.html> (accessed on 25 april 2012). *Sensors*, 2014.
- [119] J. Bernhard, J. Barr, K. W. Bowyer, and P. Flynn. Near-ir to visible light face matching: Effectiveness of pre-processing options for commercial matchers. In *IEEE International Conference on Biometrics Theory, Applications and Systems*, pages 1–8, 2015.
- [120] R. S. Ghiass, H. Bendada, and X. Maldague. Université laval face motion and time-lapse video database (ul-fmtv).
- [121] D. Kang, H. Han, A.K. Jain, and S.W. Lee. Nighttime face recognition at large standoff: Cross-distance and cross-spectral matching. *Pattern Recognition*, 47(12):3750 – 3766, 2014.
- [122] F. Jiang, P. Liu, and X. Zhou. Multilevel fusing paired visible light and near-infrared spectral images for face anti-spoofing. *Pattern Recognition Letters*, 128:30 – 37, 2019.
- [123] F. Jiang, P. Liu, X. Shao, and X. Zhou. Face anti-spoofing with generated near-infrared images. *Multimedia Tools and Applications*, 2020.
- [124] H. Steiner, A. Kolb, and N. Jung. Reliable face anti-spoofing using multispectral swir imaging. In *International Conference on Biometrics*, pages 1–8, 2016.